Postprint

Conformational dynamics of the lipopolysaccharide from *Escherichia coli* O91 revealed by NMR spectroscopy and molecular simulations

Pilar Blasco Morales,[1,§] Dhilon S. Patel,[2,§] Olof Engström,[1] Wonpil Im[2,*] and Göran Widmalm[1,*]

[1] Department of Organic Chemistry, Arrhenius Laboratory, Stockholm University, SE-106 91 Stockholm, Sweden

[2] Department of Biological Sciences and Bioengineering Program, Lehigh University, Bethlehem, PA 18015, USA

[§] Equal contribution.

[*] Correspondence: wonpil@lehigh.edu or goran.widmalm@su.se

Abstract

The outer leaflet of the outer membrane in gram-negative bacteria contains lipopolysaccharides (LPS) as a major component, and the outer membrane provides a physical barrier and protection against hostile environments. The enterohemorrhagic *E. coli* of serogroup O91 has an O-antigen polysaccharide (PS) with five sugar residues in the repeating unit (RU) and the herein studied O-antigen PS contains ~10 RUs. ^{1}H,^{13}C-HSQC-NOESY experiments on a [1-^{13}C]-labeled PS were employed to deduce ^{1}H,^{1}H cross-relaxation rates and transglycosidic $^3J_{CH}$ related to the ψ torsional angles. Dynamical parameters were calculated from the molecular dynamics (MD) simulations of the PS in solution and compared to those from ^{13}C NMR relaxation studies. Importantly, the MD simulations are able to reproduce dynamical behavior of internal correlation times along the PS chain. Two-dimensional free energy surfaces of glycosidic torsion angles delineate the conformational space available to the O-antigen. Although similar with respect to populated states in solution, the O-antigen in LPS bilayers have more extended chains as a result of spatial limitations due to close packing. Calcium ions are highly abundant in the phosphate-containing core region mediating LPS-LPS association crucial for maintaining bilayer integrity, and the negatively charged O-antigen promotes a high concentration of counterbalancing potassium ions. The ensemble of structures present for the PS in solution are captured by the NMR experiments and the similarities between the O-antigen on its own and as a constituent of the full LPS in bilayer environment makes it possible to realistically describe the LPS conformation and dynamics from the MD simulations.

Introduction

Bacteria can be classified as either gram-positive or gram-negative; the former has one plasma membrane and the latter has two cell membranes.[1] Lipopolysaccharides (LPS) abound in the outer leaflet of the outer membrane (OM) of gram-negative bacteria.[2] An LPS is comprised of lipid A that anchors the amphiphilic molecule in the membrane, a core oligosaccharide region that is relatively conserved and consists of about a dozen sugar residues and an immunogenic O-antigen polysaccharide (PS) being made of oligosaccharide repeating units (RUs), typically 5 – 25.[3,4] The biosynthesis of the PS takes place in different ways, depending on the serogroup and bacterial species, but a repetitive structure can still be identified. In the Wzy polymerase-dependent pathway an undecaprenyl-PP-sugar molecule (PP corresponds to pyrophosphate) on the cytoplasmic side of the inner membrane is used as an acceptor in the synthesis of an oligosaccharide, which then is flipped to the periplasmic side of the membrane and subsequently polymerized resulting in an O-antigen PS.[5] The number of sugar residues in a RU is usually 3 – 6 and the structure can be linear or branched depending on the way that the polymerization is carried out. This sequence of events is followed by ligation of the O-antigen to the lipid A-core molecule by WaaL, LPS transport and finally insertion in the outer leaflet at the cell surface carried out by the Lpt machinery (*LP*S *t*ransport).[6]

Changes in the growth conditions of bacteria influence the phenotypic expression of surface determinants such as rough (absence of O-antigen PS) to smooth (presence of O-antigen PS) LPS. In addition, there are presently > 180 different serogroups in *E. coli* based on the O-antigen RU sequences, and such diversity arises from different sugar components, linkages and absence or presence of branches as well as substituents such as *O*-acetyl groups.[7] Some studies suggest that different LPS structures (rough or smooth) induce differential expression levels of tumor necrosis factor-α (TNF-α) and interferon-β (IFN-β) due to differences in LPS-binding proteins (LBPs), cluster of differentiation-14 (CD14) and toll-like receptor 4 (TLR4)-dependent signaling.[8,9,10] Thus, the heterogeneity of core structures as well as O-antigen unit length and sequence variety determines antigenic diversity of bacteria. This structural diversity of LPS also creates different dynamic protein-LPS and LPS-LPS interactions and is responsible for differential OM permeability and access for antibodies to respective epitopes.[11] Molecular level insight of these structural dynamics and interactions should also be beneficial for better understanding of antibiotic resistance.[12,13,14]

This bacterium is a benign commensal, except when it has acquired DNA elements encoding for toxins; infection with pathogenic *E. coli* can be responsible for enteric/diarrhoeal disease, urinary tract infection and sepsis/meningitis. Several pathotypes have been described for *E. coli* and one of them is enterohemorrhagic *E. coli* (EHEC) causing diarrhoea with life-threatening complications, which includes serogroup O91.[15] All O-antigens from *E. coli* hitherto described have either an *N*-acetyl-D-glucosamine or an *N*-acetyl-D-galactosamine residue at its reducing end of the biological RU.[16,17] The O-antigen PS from *E. coli* O91 consists of a pentasaccharide RU (Figure 1): the commonly occurring hexopyranoses glucose, galactose, glucuronic acid (with the amino acid glycine linked to its C6), *N*-acetyl-D-glucosamine, and the unusual sugar 3-amino-3-deoxyquinovose (with the amide-linked substituents (*R*)-3-hydroxybutyric acid attached to its C3). The *E. coli* O91 RU sequence is →4)-α-D-Qui*p*-3-*N*-[(*R*)-3-hydroxybutyramido]-(1→4)-β-D-Gal*p*-(1→4)-β-D-Glc*p*NAc-(1→4)-β-D-Glc*p*A-6-*N*-Gly-(1→3)-β-D-Glc*p*NAc-(1→, where Qui*p* corresponds to 6-deoxy-glucopyranose, Gal*p* to galactopyranose, Glc*p* to glucopyranose, Glc*p*A to

glucopyranuronic acid, Gly to glycine and Glc*p*NAc to 2-acetamido-2-deoxy-glucopyranose; this structure also represents its biological RU with an *N*-acetyl-D-glucosamine residue at its reducing end. The structure determination of the O-polysaccharide was carried using ^{13}C-isotope labeling based on growths supplemented with D-[UL-[13]C$_6$]glucose, D-[1-^{13}C]glucose or D-[6-^{13}C]glucose.[18] By utilizing the site-specifically labeled materials it was possible to determine dynamics of the constituent sugars in the PS as well as the dynamics of the exocyclic hydroxymethyl groups of three of the sugars of the RUs.[19,20] Also, NMR data facilitated the determination of the chain length of the polymer to be ~10 repeating units, which was consistent with a narrow distribution deduced from a MALDI-TOF mass spectrometry experiment.

The three-dimensional structure of these O-antigens is recognized by antibodies and an understanding of their conformation and dynamics is a prerequisite for further developments in the design of carbohydrate-based vaccines.[21,22] The conformation can be assessed by molecular modeling techniques,[23] preferably in combination with NMR spectroscopy that gives atomic-resolution information,[24,25] and further insights to their conformational behavior can be gained by carrying out molecular dynamics (MD) simulations.[26,27,28,29] We herein carry out NMR-based nuclear Overhauser effect (NOE) experiments on the ^{13}C-isotope labeled O-antigen from *E. coli* O91 in isotropic water solution. In this way resolved NMR spectra can be obtained alleviating severe overlap present in homonuclear ^{1}H-based NMR spectra of natural abundance material. In addition, the ^{13}C-isotope labeling scheme facilitates measurements of heteronuclear transglycosidic coupling constants that report on conformational preferences at the glycosidic linkages of the polymer. Experimental NMR data are then compared with extensive MD simulations of the O-antigen PS *per se*, i.e., in solution, and of the LPS with five or ten RUs in a membrane environment representing the outer leaflet of *E. coli* O91. Specific aims of the study include investigation of whether the current generation of a carbohydrate force field is able to reproduce experimental data, herein acquired by NMR spectroscopy, and subsequently similarities and differences of an O-antigen PS free in solution in comparison to when it is part of the LPS in a membrane environment.

Materials and Methods

NMR experiments

The NMR experiments were performed on *E. coli* O91 O-antigen PS preparations in D$_2$O using either a natural abundance sample (16.5 mg in 0.55 mL) or a [1-^{13}C]-labeled PS (2 mg in 0.55 mL); to this end the materials were treated with CHELEX-100 resin, filtered and transferred to 5 mm NMR tubes. ^{1}H and ^{13}C NMR chemical shifts were referenced to external 3-trimethylsilyl-(2,2,3,3-[2]H$_4$)-propanoate (TSP, δ_H 0.00 ppm) and 1,4-dioxane in D$_2$O (δ_C 67.40 ppm). Most ^{1}H and ^{13}C NMR chemical shift assignments were available from literature.[18]

A 700 MHz Bruker AVANCE III spectrometer equipped with a TCI Z-Gradient cryoprobe was used for experiments at 310 K, where the temperature had been calibrated with a sample of neat deuterated methanol.[30] On the natural abundance sample 1D-selective ^{1}H,[1]H-NOE experiments with zero-quantum coherence suppression[31] were performed with a relaxation delay of 4.0 s by selective irradiation with a 100 ms r-SNOB shaped pulse at the resonance frequency of the anomeric proton of residue E (Qui3NAcyl in Figure 1) at 4.90 ppm. The spectra were acquired with 16k data points and nine mixing times from 60 to 160 ms.

^{1}H,^{13}C-HSQC-NOESY experiments[32] on the [1-^{13}C]-labeled PS were performed with an 80 kHz smoothed Chirp pulse (0.5 ms, 20.1% smoothing) for the initial and final ^{13}C pulses of the pulse

sequence and a broadband GARP4 ^{13}C-decoupling sequence. The spectra were acquired with 256 × 2k data points, spectral widths of 25 × 7 ppm in the F_1 and F_2 dimensions, respectively, and a relaxation delay of 10.2 s. Nine experiments were performed with varying mixing times from 40 ms to 600 ms. Peak volumes in the two-dimensional (2D) spectra were integrated for auto- and cross-peaks to construct NOE buildup curves[33] followed by the PANIC approach,[34,35] in which every cross-peak volume at each mixing time was divided by its corresponding auto-peak volume of the anomeric resonance. The fitting of the PANIC data by a first order function was used to calculate the cross-relaxation rates. ^{1}H,^{13}C-Heteronuclear transglycosidic coupling constants were obtained from phase-sensitive ^{1}H,^{1}H-NOESY spectra of [1-^{13}C]-labeled *E. coli* O91 PS acquired using four mixing times (40, 60, 80 and 100 ms), 256 × 8k data points in the F_1 and F_2 dimensions, respectively, a spectral width of 6 ppm and a relaxation delay of 9.9 s.

Analysis of NMR data

Proton-proton distances were obtained from cross-relaxation rates (σ) employing the isolated spin-pair approximation (ISPA)[36] and an intraresidue effective reference distance of 2.39 Å for the spin-pair E1-E2, having $\sigma = 2.38$ s^{-1}, where the distance was taken from the MD simulation of the O-antigen PS in solution (PS10; see below for the details), omitting the first and last repeating units of the polymer for the analysis. Errors in σ were calculated using the jackknife procedure[37] and are reported as one standard deviation (SD). Based on ±1 SD errors were subsequently estimated for the experimentally determined proton-proton distances. Constraints employed in the fitting procedure were that the y-axis intercept should be within 5% of the value at the longest mixing time and the correlation coefficient $R^2 > 0.9$. A final visual inspection of the PANIC plots reassured the quality of the fitting procedure. Karplus-type equations developed for transglycosidic spin-spin coupling constants[38] were used for the calculations of $^3J_{CH}$ from the MD simulations.

Molecular Dynamics Simulations

System setup

For the MD simulation of the PS in solution, an initial PS conformation containing 10 RUs of the O-antigen (PS10) was generated from the topology information present in the CHARMM force field[39,40,41,42] and subjected to a brief energy minimization using steepest descent and adopted basis Newton−Raphson methods. Three PS10 solution simulation systems were built independently using *Glycan Reader* and Quick MD Simulator utility in CHARMM-GUI (http://www.charmm-gui.org).[43,44] The system size was determined to have at least a 12.5 Å water layer in every direction. The solution simulation systems were energy minimized with the positional harmonic restraint applied to the non-hydrogen atoms of PS10 using CHARMM simulation software.[45] The solvated PS10 systems contained ~231,000 atoms.

Building and assembly of two LPS bilayer systems LPS5 (lipid A + R1 core + 5 RUs of O-antigen) and LPS10 (lipid A + R1 core + 10 RUs of O-antigen) (Figure 2) were achieved by the step-by-step protocol previously used in LPS simulations[11,27,46,47] and based on the well-established protocol in CHARMM-GUI *Membrane Builder*[43,48,49,50] These building steps were repeated three times with different random seed numbers to generate three independent replicas to improve sampling and to check for simulation convergence. The solvated LPS5 and LPS10 systems contained ~192,000 and ~305,000 atoms, respectively. For LPS5 and LPS10 bilayer systems, we used the Ca^{2+} ions and restricted their initial placement to neutralize all the negative charge on the Lipid A head groups and of the core sugar residues (Kdo: 2-keto-3-deoxy-D-*manno*-octulosonate and phosphorylated Hep: L-

glycero-D-*manno*-heptose). K^+ ions are used to neutralize the negative charge of O-antigen in LPS bilayer systems as well as solution systems. In addition 150 mM KCl was used for bulk ionic solution at the start of simulations for LPS bilayer systems while no extra bulk ions were added for solution systems. For all three ions, 2000 steps of Monte Carlo simulations were performed to obtain their initial positions.

Simulation protocol

The energy minimized PS10 solution systems were subjected to 50 ps each of NVT (constant particle number, volume, and temperature) and NPT (constant particle number, pressure, and temperature) equilibration using CHARMM followed by 400 ns of NAMD production simulations at 300 K. Similarly, LPS5 and LPS10 membrane systems were equilibrated for 450 ps using CHARMM;[45] Langevin temperature control was used for NVT dynamics, and a Hoover thermostat[51] and Langevin piston were used to control temperature and pressure for NPT dynamics.[52,53] This was followed by 400-ns NPT production runs with NAMD[54] where the NAMD input scripts had been generated by CHARMM-GUI.[55] This resulted in a total simulation time of 1.2 μs for each PS10, LPS5, and LPS10 system. During LPS5 and LPS10 equilibration, various planar and dihedral restraints were applied to the LPS molecules and water molecules; these restraint forces were gradually reduced to zero for the production simulations.[46,47] Additional dihedral angle restraints were applied to restrain all sugar rings to the pertinent chair conformation, which were maintained during the production simulations in both solution and membrane simulation systems. The temperature and pressure were held at 310.15 K and 1 bar, respectively, for the membrane systems. In NAMD production runs, Langevin dynamics was used to maintain constant temperature with a Langevin coupling coefficient of 1 ps^{-1}, and a Nosé-Hoover Langevin piston[56,57] was used to maintain constant pressure with a piston period of 50 fs and a piston decay time of 25 fs while keeping barostating isotropic for the PS10 solution system and anisotropic for both LPS5 and LPS10 systems. A 2-fs timestep was used for integration together with the SHAKE algorithm,[58] where all covalent bonds between hydrogen and the heavy atom are constrained. The van der Waals interactions were smoothly switched off at 10 – 12 Å by a force-switching function,[59] while the long-range electrostatic interactions were calculated using the particle-mesh Ewald method.[60] All the systems (solution and membrane) were simulated with the CHARMM36 (C36) force field for lipids,[61] carbohydrates[39,40,41,42] and LPS,[27] using the TIP3P water model.[62] In addition, the force field parameters of two chemically modified sugars (α-D-Qui3NAcyl and β-D-GlcA6NGly) were manually assigned by analogy with the C36 carbohydrate force field[39,40,41,42] used in this study.

Computation of NMR relaxation parameters

The relaxation parameters can be expressed in terms of spectral density functions, $J(\omega)$, taken at different combinations of the carbon (ω_C) and proton (ω_H) Larmor frequencies. The longitudinal relaxation time T_1 is related to the spectral densities by the following:[63,64]

$$T_1^{-1} = \frac{b^2}{4}\left[J(\omega_H - \omega_C) + 3J(\omega_C) + 6J(\omega_H + \omega_C) \right] \tag{1}$$

where $b = (\mu_0/4\pi)\gamma_C\gamma_H\hbar r_{CH}^{-3}$, μ_0 is the permittivity of free space, γ_C and γ_H are the magnetogyric ratios for carbon and proton, respectively, $\hbar$ is Planck's constant divided by 2π, and $r_{CH} = 1.117$ Å

is the carbon-hydrogen bond length. Dynamical processes relevant for the spin relaxation parameter are described by $J(\omega)$:[65]

$$J(\omega) = \frac{2}{5} \int_0^\infty \langle P_2[\mu(0) \cdot \mu(t)] \rangle (\cos \omega t) \, dt \qquad (2)$$

where μ is a vector undergoing reorientation and $P_2(x) = (3x^2 - 1)/2$ is the second rank Legendre polynomial. In order to analyze the experimental T_1 relaxation parameter a functional form of $J(\omega)$ is required. Employing the model-free formalism pioneered by Lipari and Szabo[65] $J(\omega)$ is modeled as:

$$J(\omega) = \frac{2}{5} \left[\frac{S^2 \tau_M}{1 + (\omega \tau_M)^2} + \frac{(1 - S^2)\tau}{1 + (\omega \tau)^2} \right] \qquad (3)$$

where $\tau^{-1} = \tau_e^{-1} + \tau_M^{-1}$, S^2 is the square of the generalized order parameter which reflects the spatial restriction of local motion, τ_e is the correlation time for internal motions and τ_M is the correlation time for the global reorientational motion.

From the PS10 solution simulations the reorientational correlation function $C(t) = \langle P_2[\mu(0) \cdot \mu(t)] \rangle$ was obtained for the C1-H1 vector of the sugar residues and in each case it was fitted to a bi-exponential form:[66]

$$C(t) = (1 - S^2) \exp(-t/\tau_e) + S^2 \exp(-t/\tau_M) \qquad (4)$$

where τ_e and τ_M are the decay times of rapid and slow motions, respectively. The fitting of the decaying correlation function was carried out to each 12-ns piece of the three 400-ns trajectories from which the averages and SD were calculated.

Results and Discussion

NMR experiments

The primary structure of the O-antigen of *E. coli* O91 was previously determined mainly by NMR spectroscopy making use of different ^{13}C-labeling schemes thereby facilitating application of NMR experiments not feasible on natural abundance material.[18] In order to be able to easily refer to aspects and results from the previous studies we continue to use to the original designation of the sugar residues denoted by A – E (Figure 1). The ^{1}H and ^{13}C NMR chemical shift assignments at 338 K were thus available from the previous study and minor chemical shift displacements besides those already documented in ^{13}C NMR relaxation studies at 310 K for [1-^{13}C]- as well as [6-^{13}C]-labeled *E. coli* O91 PS[19,20] were readily accounted for by standard 2D NMR experiments. The NMR chemical shift assignments of H6$_{pro-R}$ and H6$_{pro-S}$ of the hydroxymethyl group in the galactose residue (A) were obtained by a ^{1}H,^{1}H-NOESY NMR experiment[67] considering the NOEs between H4 and the two hydroxymethyl group protons in conjunction with the anticipated rotameric distribution at the ω torsion angle of galactose.[68]

^{1}H,^{1}H-NOESY NMR experiments facilitate determination of proton-proton cross-relaxation rates, usually performed by acquiring NOE buildup curves based on several experiments with different

mixing times, and subsequently deriving interproton distances by ISPA.[33,36] In the ^{1}H NMR spectrum of the *E. coli* O91 PS the anomeric proton of the α-linked residue E is well resolved, whereas the anomeric protons of the β-linked residues A – D are completely overlapped (Figure 3A) thereby impeding a quantitative analysis based on the standard 2D ^{1}H,^{1}H-NOESY NMR experiment. Selective excitation of nuclei whose resonances are resolved in the NMR spectrum is possible by employing a shaped pulse targeting the desired resonance frequency.[69] This approach was applied in a 1D ^{1}H,[1]H-NOESY experiment where NOEs were observed from proton E1 interresidually to protons A4, A5, A6$_{pro-R}$ and A6$_{pro-S}$ as well as intraresidually to E2 (Figure 3B); the latter was chosen as the reference distance in order to determine experimentally derived proton-proton distances in the polymer. An NOE buildup curve, analyzed by the PANIC approach,[34,35] was used to determine cross-relaxation rates between proton pairs and subsequently distances by ISPA (Table 1).

Using ^{13}C-labeling of PS efficient NMR experiments can be applied for assigning resonances of NMR-active nuclei in carbohydrates, including those giving sequence information between sugar residues.[70] In studies of the cell wall PS from *Streptococcus mitis* J22 uniform ^{13}C-labeling of the PS was performed thereby enabling 2D ^{1}H,[1]H-NOESY and 3D ^{1}H,[13]C-HMQC-NOESY experiments to be carried out, which gave information on NOE contacts and transglycosidic heteronuclear coupling constants.[71,72,73] The ^{13}C NMR resonances of the anomeric carbons from residues A – E are resolved and by using the [1-^{13}C]-labeled *E. coli* O91 PS in 2D ^{1}H,^{13}C-HSQC-NOESY experiments it was possible to integrate most cross-peak volumes individually in spectra (Figure 3C) having different mixing times. However, ^{1}H NMR chemical shifts of E4 and C5 resonate at ~3.45 ppm and the NOEs from the anomeric proton C1 thus overlap also in the HSQC-NOESY spectra. Since the proton-proton NOE for the C1-C5 NOE is intraresidual and the effective distance can be estimated very well from the MD simulations its cross-relaxation rate can be determined and the contribution to the apparent C1-E4/C5 cross-relaxation rate be known. Following subtraction of the C1-C5 cross-relaxation rate from the apparent one leads to the cross-relaxation rate of C1-E4 (Table 1). This approach was previously used,[74] validated[75] and has been shown to be efficient for extracting distance information from cross-relaxation rates, in particular when resonances giving rise to intraresidual NOEs overlap in spectra with a resonance leading to an interresidual NOE of unknown distance.[76] Subsequently, NOE buildup curves were constructed and analyzed by the PANIC approach (Figure 4) to give cross-relaxation rates and interproton distances (Table 1).

Three-bond coupling constants across the glycosidic linkage offer information on conformational preferences of the constituent sugar residues and the torsional angles related to ϕ and ψ. These $^3J_{CH}$ and $^3J_{CC}$ couplings are interpreted by Karplus-type relationships specifically developed to this end.[38] For oligosaccharides the *J* coupling constants can be determined by e.g. J-HMBC experiments.[77,78] However, for PS of considerably higher molecular mass these techniques are not suitable due to long coupling evolution delays during the experiments and other means of determining the *J* couplings are required. In the study of the *S. mitis* J22 cell wall PS Bush and co-workers utilized the 2D ^{1}H,[1]H-NOESY experiment to determine transglycosidic $^3J_{CH}$ couplings in the uniformly ^{13}C-labeled material.[71] Having access to the [1-^{13}C]-labeled *E. coli* O91 PS we focus on the fact that a $^3J_{C1',Hn}$ coupling from the anomeric carbon of one residue to the proton of the glycosyloxylated carbon, i.e., the linkage carbon atom, is anticipated and its magnitude should give information on preferred conformations related to the ψ torsion angle at each glycosidic linkage.

The anomeric proton resonance of each residue is split by the large $^1J_{C1,H1}$ coupling. In the 2D ^{1}H,^{1}H-NOESY spectrum the peak displacement, in Hz, along the F$_2$ dimension of the two cross-peaks between H1' and Hn of the subsequent sugar residue (Figure 5) reports on the $^3J_{C1',Hn}$ coupling. These types of coupling constants were possible to determine for three out of the five residues and were quite large, in the range 5 – 6 Hz (Table 2); one may note that the maximum $^3J_{CH}$ coupling constant for syn- and antiperiplanar orientations is the range 6 – 8 Hz.[38]

Comparison with MD simulations

The results from the NMR experiments can be compared with those calculated from MD simulation trajectories to validate the simulation (and thus the empirical molecular mechanics force field); once validated one can reliably extend the analysis of the simulation to gain insight into structural aspects and dynamical processes. For the comparisons we initially rely on the MD simulation of the O-antigen PS with ten RUs (PS10) solvated in water since it should be most representative to this end, but further analysis of the LPS5 and LPS10 membrane systems was also done to examine the similarities or differences to data from PS10 in solution to address the environmental influences on PS structure and dynamics.

In this study comparison of experimental NMR data to those calculated from the MD simulations is based on effective proton-proton distances, transglycosidic heteronuclear coupling constants and ^{13}C T_1 spin-lattice relaxation times. Having obtained the ^{1}H,^{1}H cross-relaxation rates from the NOESY experiments and choosing a reference intraresidual E1-E2 distance from the MD simulation according to $1/r_{eff} = \left\langle r_{MD}^{-6} \right\rangle^{1/6}$, the unknown distances in the molecule can be derived by ISPA. In other words, the unknown distance r_{ij} can be determined from the relationship $r_{ij} = r_{ref} \left(\sigma_{ref}/\sigma_{ij} \right)^{1/6}$ where r_{ref} is the known reference distance from the MD simulation, σ_{ref} and σ_{ij} are the cross-relaxation rates for the reference interaction and the interaction between spins i and j, respectively.[36] The PS10 behaves as a random coil polymer sampling all orientations (Figure 7) and this fact forms the basis for analyzing the NOE data using an isotropic model. Based on the reference distance intraresidual distances were analyzed in other sugar residues and were found to be consistent with the MD simulations with deviations of < 0.2 Å (Table 1, Figure 6).

The experimentally determined transglycosidic distances for the E1-A4 and E1-A6$_{pro-S}$ pairs were obtained from a 1D ^{1}H,^{1}H-based NOESY experiment using the natural abundance PS, resulting in $r_{ij} \approx 2.6$ Å for both, which is longer than $r_{ref} = 2.39$ Å. In the subsequent analysis based on the HSQC-NOESY experiments of the [1-^{13}C]-labeled PS these proton-proton distances differed by < 0.1 Å from those determined by the 1D experiment, thereby validating the 2D NMR approach relying on the ^{13}C isotope enrichment. Transglycosidic distance information from the anomeric proton to the proton at the glycosyloxylated position was in this way possible to obtain for all five linkages (Table 1, Figure 6). For the C1-E4 pair the agreement is excellent for the PS10 simulation, whereas the distance is slightly longer for the two LPS simulations. The agreement is good, but reversed for the transglycosidic pair D1-B4, i.e., LPS simulations agree slightly better than the PS10 simulation. For interactions between anomeric protons and those not at the linkage position, agreement vary from excellent for the E1-A6$_{pro-S}$ pair to good for D1-B5 and C1-E5, though being dependent on whether the LPS or the PS simulations are used for the two latter comparisons. For the A1-D4 and B1-C3 pairs the experimentally determined transglycosidic distances are somewhat

longer than what is observed from the MD simulations. Both pairs are part of β-D-hexoses linked to an oxygen atom at a secondary carbon atom. From the free energy surfaces of the glycosidic linkages (Figure 8) it is evident that anti-ψ conformational states are also populated, i.e., Q3 for the glycosidic linkage of A-D and Q2 for that of B-C. A larger population, though still < 10%, will give good agreement between experiment and simulation, supporting the notion of conformational flexibility within the PS.

The α-linked residue E connected to position O4 of residue A also shows a longer E1-A4 transglycosidic distance between the anomeric proton and the proton at the linkage position. However, instead of a single-well major conformational state and a minor anti-ψ state with significantly less populated than the four β-linked residues, the α-linked E residue shows a syn-conformation with a bistable potential along the ψ torsion in all three simulations and a negligible contribution from an anti-ψ state (Figure 8, Figures S1 and S2). The effective E1-A4 distance for the two states was analyzed separately and found to be $r_{eff} = 2.15$ Å and $r_{eff} = 2.24$ Å in the Q4$^{(syn+)}$ and Q4$^{(syn-)}$ states, corresponding to ψ_H being positive or negative (Figure 9). Thus, a higher population of the Q4$^{(syn-)}$ state would lead to a slightly better agreement with experimental data. However, the deviation from experiment (Table 1) is still significant and it is evident from NMR spectra that the transglycosidic E1-A4 distance is longer than the intraresidue reference distance E1-E2 (cf. Figure 3b and Figure 4). This bistable potential along the ψ torsion angle is closely similar to the α-D-Glc*p*NAc-(1→4)-D-Gal*p* structural element present in the O-antigen of *E. coli* O6 connecting the biological RUs of the PS, previously analyzed by NMR spectroscopy and MD simulations.[46] In that study the conformational space was in a very similar way described by a two-well distribution and the minor conformational state in the MD simulation, with a negative value of its ψ_H torsion angle, should be the preferred one in order to obtain better agreement between simulation and experiment. These two cases indicate that the structural element α-D-Hex*p*-(1→4)-D-Gal*p* (where Hex is a hexose residue), as a disaccharide or present in larger oligosaccharides, would benefit from a detailed investigation of its conformational preferences and dynamics when described by the CHARMM36 (C36) force field; NMR spectroscopy would then be highly suitable experimental technique for supplying experimental data for fine-tuning of the torsional potentials at this linkage, in a similar way that recently was performed for (1→6)-linkages between hexopyranosides.[42]

The other experimental source of information about glycosidic torsion preferences in the PS was herein obtained from the $^3J_{CH}$ coupling constants related to the ψ torsional angles as a result of the ^{13}C-labeling of the anomeric carbon atoms. While the major conformational state at the ϕ torsion angle of carbohydrates is governed by the *exo*-anomeric effect the preference at the ψ torsion angle is dependent on steric effects[79] and to some extent also interresidual hydrogen bonding.[80] The ability of obtaining additional conformation-related information for the latter torsion via $^3J_{CH}$ couplings is very valuable. From the MD simulations $^3J_{CH}$ values were calculated using Karplus-type relationships[38] and for three out of the five torsions the experimentally determined values were possible to compare with the simulated ones (Table 2). The $^3J_{CH}$ coupling related to ψ_{E-A} is smallest in magnitude and the agreement with the simulations is excellent. Notably, the calculated couplings from the Q4$^{(syn+)}$ and Q4$^{(syn-)}$ conformational states bracket the one observed experimentally, indicating that averaging takes place at the ψ_{E-A} torsion angle. The largest value was observed for

$^3J_{CH}$ related to $\psi_{C\text{-}E}$, which is also in excellent agreement to the PS10 simulation and the result is consistent with a small population of an anti-ψ conformer, i.e., population of the Q3 quadrant in addition to the major population in the Q2 quadrant (Figure 8). The $^3J_{CH}$ value related to the $\psi_{A\text{-}D}$ torsion was intermediate to the other ones both from experiment and simulation, supporting the synperiplanar conformational state in the Q2 quadrant as the major one. Analysis of the conformational preference of the $\phi/\psi_{A\text{-}D}$ in the Protein Data Bank (Figure S3) revealed that there is a population distribution (of 540 glycan structures identified using Glycan Fragment DB[81] available at http://glycanstructure.org/fragment-db) very similar to that observed for $\phi/\psi_{A\text{-}D}$ PS10 simulation. This result suggests that inherent conformational preferences for synperiplanar $\psi_{A\text{-}D}$ in solution are also retained in other sugar chains, while some of the structures show accessibility of high-energy anti-ψ conformers. Structural analysis of β-D-Gal$p$-(1→4)-β-D-Glc$p$NAc disaccharide units of PS10 shows synperiplanar $\psi_{A\text{-}D}$ conformers stabilized by interresidual H-bonding interactions between O5$_A$···HO3$_D$, whereas no such preferential stabilization by interresidual H-bonding is observed for anti-$\psi_{A\text{-}D}$ conformers (Figure S4). Similarly, synperiplanar $\psi_{C\text{-}E}$ and $\psi_{D\text{-}B}$ conformers show stabilization with one or more interresidual H-bonding interactions, while they are absent in anti-ψ conformers for β-D-Glc$p$NAc-(1→4)-α-D-Qui$p$-3-N-[(R)-3-hydroxybutyramido] and β-D-Glc$p$NAc-(1→4)-β-D-Glc$p$A-6-N-Gly disaccharide units of PS10.

The use of a singly ^{13}C-labeled site within the pyranose ring of each sugar residue suffices to reveal dynamical information on the ps-ns time scale and, in contrast to e.g. uniformly labeled carbon-13 material, alleviates the need to consider additional relaxation and spin-spin couplings to other ^{13}C-labeled sites within the saccharide. The [1-^{13}C]-labeled $E.\ coli$ O91 PS had previously facilitated the acquisition of ^{13}C NMR relaxation data at two magnetic field strengths for the following parameters: T_1 spin-lattice and T_2 spin-spin relaxation times as well as ^{1}H,^{13}C NOEs.[19] Subsequent analysis employing the model-free approach[65] resulted in a description of dynamical parameters such as S^2 reflecting spatial restriction of local motion, τ_e describing the correlation time for internal motions and τ_M specifying the correlation time for global motion (see Eqn. 4). Herein the dynamics of the C1-H1 vector in each of the five sugar residues A – E for RU 2 – 9 of PS10 was analyzed from the MD simulation by calculating the correlation function $C(t) = \left\langle P_2 \left[\mu(0) \cdot \mu(t) \right] \right\rangle$ and subsequently fitting it to the bi-exponential function described by Eqn. 4, which facilitated extraction of S^2, τ_e and τ_M (Table 3). In comparison of dynamical and NMR relaxation parameters obtained from the MD simulations one often has to consider the viscosity of the water model (TIP3P) used in the simulations and that present under the experimental conditions of the NMR experiments,[69] e.g., in this case the solute molecule is dissolved in D$_2$O. It is well-known that the TIP3P water model has a lower viscosity than that experimentally determined for water.[82] Furthermore, the viscosity of D$_2$O is slightly higher than that of H$_2$O.[83] Herein, we decided to proceed directly from the MD simulations *per se*, since the analysis of trends in the data is of prime interest for the PS dynamics (*vide infra*).

The computed S^2 values from the simulations are generally slightly lower than those determined from experiment revealing a dynamic polymer, in agreement with experimental results. In the interpretation of the ^{13}C NMR relaxation data the model-free approach employs an overall correlation time for the global motion, which was experimentally determined as $\tau_M = 5.42$ ns. From

the MD simulations the τ_M values are of similar magnitude, which is of importance in calculating T_1 relaxation times, without taking scaling due to viscosity differences into account. The correlation times for internal motions τ_e of the various sugar residues calculated from the MD simulations show, when scaled by τ_M^{NMR}/τ_M^{MD}, that the sequentially connected sugar residues –C-E– have similar and longer τ_e values than those in the sequence –A-D-B– with shorter and comparable τ_e values (Table 3). Most interestingly, the MD simulations, in conjunction with an overall scaling of correlation times, are able to reproduce this dynamical behavior along the PS chain, thereby giving credence to the model produced by using the empirical C36 carbohydrate force field. Subsequent calculation of T_1 relaxation times using dynamical parameters from the MD simulations (without scaling) together with Eqns. 1 and 3 resulted in relaxation data similar to those observed experimentally and, in particular, that trends in relaxation times are captured (Table 3).

The terminal repeating unit of the polysaccharide is from NMR data known to be more flexible[19] and the reducing end repeating unit linked to the core region is also anticipated to show different dynamics than the remaining parts of the polysaccharide. This is the basis for choosing repeating units 2 – 4 and 2 – 9 when performing analysis of MD data. The conformational dynamics along the polymer chain was captured by the MD simulation, which was able to describe ^{13}C NMR relaxation parameters. Furthermore, the heteronuclear long-range coupling constants and their relative magnitudes were possible to account for as well as most of the effective proton-proton distances obtained from ^{1}H,^{1}H-NOESY experiments. The description of a dynamic polysaccharide with major well-defined conformational states and to some extent populated anti-ψ conformers leads from a physical point of view to a picture where saccharide epitopes can be recognized, e.g., LacNAc (residues A-D) by lectins and antibodies but also that it will be able to attain different conformational population distributions when the physical environment changes, such as when present in a LPS bilayer.

Structure and dynamics of LPS molecules in a bilayer

The 2D free energy surfaces of the glycosidic torsion angles from the LPS5 and LPS10 simulations (Figures S1 and S2) are quite similar to those from the PS10 simulations (Figure 8). Some differences can, however, be identified on going from the PS10-only to the bilayer simulations, e.g., for both the C-E and D-B linkages an increase in anti-ψ_H conformations is observed, i.e., Q3 becomes more populated at the expense of Q2. Furthermore, for the E-A linkage with the Q4$^{(syn+)}$ and Q4$^{(syn-)}$ states, corresponding to ψ_H being positive or negative, respectively, the major conformational state is shifted from Q4$^{(syn-)}$ for PS10 to favoring the Q4$^{(syn+)}$ state for LPS10. Thus, although the packing of the LPS in the bilayer brings about spatial and consequently conformational restrictions to the O-antigen the MD simulations indicate that conformations accessible, but less populated, in PS-only solution become increasingly populated when present in a bilayer environment.

To obtain general perspectives of how the PS conformational dynamics affect structural packing and dynamics of LPS molecules in a bilayer and its dependence on the LPS molecular length, we calculated heavy atom density profiles along the Z-axis (i.e., the membrane normal) (Figure 10). The core structures as well as the different RUs in the LPS5 O-antigen are slightly more extended than the corresponding ones in LPS10. This is consistent with our observation in the previous study with LPS5 and LPS10 bilayers for the *E. coli* O6 O-antigen.[46] In addition, broader density

distributions of the terminal RU of the *E. coli* O91 O-antigen in both LPS5 and LPS10 suggest that these residues are less packed and possess more extensive dynamics as compared to the residues closer to the membrane center (Z=0). Structural dynamics of LPS visualized for a few selected LPS10 molecules from the simulation trajectory (Figure 11) highlight different conformations sampled while retaining more extended overall shapes. The time-averaged root-mean-square fluctuation (RMSF) for different regions of the LPS molecules also show that the order of the relative flexibility increases from the core sugars to the more flexible terminal RU (Figure S5). The terminal RU of the LPS shows a conspicuously higher flexibility than the remaining parts of the polymer, consistent with a fact that was previously deduced from ^{13}C NMR spin-relaxation data on PS10.[19] Thus, the overall structure and dynamics of LPS molecules in bilayers are influenced by the packing of the components.

Influences of LPS molecular charge, packing, and dynamics on the permeability and distribution of ions are clearly observed with calculated ion density profiles along the Z-axis (Figure 12). Like in previous LPS bilayer simulations,[46] current simulations also show a prominent distribution of Ca^{2+} ions in the region of lipid A head and core sugars. Such a distribution in this region was previously suggested to be responsible for Ca^{2+}-mediated LPS-LPS association and to be crucial for maintaining the integrity of the outer membrane structures.[84,85,86,87] A minor distribution of Ca^{2+} ions, in exchange with K^+ ions, extends outwards from the core region to counterbalance the negative charge of the glycine residues in O-antigen. Interestingly, the negatively charged O-antigen facilitates deep penetration of K^+ ions and restricted movement of Cl^- ions into the core and O-antigen regions. Some K^+ ions even interact with the head group of lipid A in the LPS bilayer, but Cl^- ions are mostly concentrated in the bulk water region. Importantly, in our previous study of the *E. coli* O6 LPS bilayer systems, which has a neutral O-antigen there was no preference for movement of K^+ or Cl^- ions into the O-antigen region.[46] For *E. coli* O91, the negatively charged O-antigen facilitates an extra layer for screening out negatively charged solute molecules in general.

Further insight into the O-antigen conformational dynamics in the LPS5 and LPS10 bilayers was gained from analysis of the distances between the lipid A phosphate groups and the first residue of each O-antigen RU along the Z-axis (Figure 13A). Consistent with the *E. coli* O6 O-antigen in the LPS5 and LPS10 bilayer systems,[46] the present one also prefers to be in extended conformations in LPS bilayers due to close LPS-LPS distances and less space available. Condensed packing of LPS molecules is also reflected in calculated average tilt angle of each O-antigen RU, showing that with inclusion of more repeating units from LPS5 to LPS10, the O-antigens are less tilted from the Z-axis (Figure 13B). Extended polymer chains as a result of molecular packing in LPS bilayers are contrasted to the varied PS10 solution conformations (extended to curved) of the O-antigen due to availability of free 3D conformational space (Figure 7). This is further evident from a time-series analysis (Figure S6) of end-to-end distance calculations between the first residue of RU1 and last residue of RU5 in LPS5 and RU10 in solution and LPS10 (Figure S6).

Conclusions

The conformational preferences and dynamics of the *E. coli* O91 O-antigen have been investigated using NMR experiments of the PS in water solution and corresponding MD simulations as well as simulation of the LPS in a bilayer environment. The severe proton spectral overlap in the O-antigen was alleviated by use of [1-^{13}C]-labeled PS form which both ^{1}H,[1]H cross-relaxation rates and transglycosidic $^3J_{CH}$ coupling constants were obtained. Derived experimental effective proton-proton distances were compared to those from a PS-only MD simulation, revealing in general good

13

agreement between experiment and simulation; where a somewhat lower agreement was observed it may be due to a slight underrepresentation of anti-ψ conformational states. The comparison of simulated transglycosidic $^3J_{CH}$ coupling was facilitated by interpretation via a Karplus-type relationship and showed, in particular, that they were reproduced very well by the force field used for the simulation. The calculation of T_1 relaxation times using dynamical parameters from the MD simulations resulted in relaxation data similar to those observed experimentally, thereby revealing, by a completely different set of experimental data and subsequent analysis, that the simulations describe well the conformational dynamics of the PS. The O-antigen as PS-only in solution is free to populate conformational space available while the LPS molecules in LPS5 and LPS10 homogeneous bilayer environments experience restricted movement from adjacent LPS molecules and are bound to retain more extended conformations. Furthermore, since the conformational space for the glycosidic linkages populated by the PS10 and the O-antigen part of LPS5 and LPS10 is similar and NMR experiments on PS-only are able to capture the ensemble of structures that exist credence is given to the LPS model in a bilayer. In contrast to the neutral *E. coli* O6 O-antigen[46] the negatively charged O-antigen of *E. coli* O91 allows deep penetration of K^+ ions to counterbalance the negative charge of the glycine residues in the O-antigen, conceivably shielding the bacterium by also an electrostatic mechanism to the external environment, besides the permeability barrier the O-antigen presents on its own. Future directions of continued research will include acquisition of NMR data for LPS in lipid membrane bilayer disc-like constructs or as natural constituents of the bacterial cell.

Acknowledgements

Supporting Information

Glycosidic ϕ/ψ torsion angle plots and analysis data from MD simulations.

References

(1) Silhavy, T. J., Kahne, D., and Walker, S. (2010) The Bacterial Cell Envelope. *Cold Spring Harb. Perspect. Biol. 2*, a000414.

(2) Rhee, S. H. (2014) Lipopolysaccharide: Basic Biochemistry, Intracellular Signaling, and Physiological Impacts in the Gut. *Intest. Res. 12*, 90–95.

(3) Ali, T., Weintraub, A., and Widmalm, G. (2007) Structural determination of the O-antigenic polysaccharide from Escherichia coli O166. *Carbohydr. Res. 342*, 274–278.

(4) Linnerborg, M., Weintraub, A., and Widmalm, G. (1999) Structural studies utilizing 13C-enrichment of the O-antigen polysaccharide from the enterotoxigenic Escherichia coli O159 cross-reacting with Shigella dysenteriae type 4. *Eur. J. Biochem. 266*, 246–251.

(5) Kalynych, S., Morona, R., and Cygler, M. (2014) Progress in understanding the assembly

process of bacterial O-antigen. *FEMS Microbiol. Rev. 38*, 1048–1065.

(6) Putker, F., Bos, M. P., and Tommassen, J. (2015) Transport of lipopolysaccharide to the Gram-negative bacterial cell surface. *FEMS Microbiol. Rev. 39*, 985–1002.

(7) Stenutz, R., Weintraub, A., and Widmalm, G. (2006) The structures of Escherichia coli O-polysaccharide antigens. *FEMS Microbiol. Rev. 30*, 382–403.

(8) Shimada, M., Kadowaki, T., Taniguchi, Y., Inagawa, H., Okazaki, K., and Soma, G. I. (2012) The Involvement of O-antigen Polysaccharide in Lipopolysaccharide in Macrophage Activation. *Anticancer Res. 32*, 2337–2341.

(9) Jiang, Z., Georgel, P., Du, X., Shamel, L., Sovath, S., Mudd, S., Huber, M., Kalis, C., Keck, S., Galanos, C., Freudenberg, M., and Beutler, B. (2005) CD14 is Required for MyD88-Independent LPS Signaling. *Nat. Immunol. 6*, 565–570.

(10) Huber, M., Kalis, C., Keck, S., Jiang, Z., Georgel, P., Du, X., Shamel, L., Sovath, S., Mudd, S., Beutler, B., Galanos, C., and Freudenberg, M. A. (2006) R-form LPS, the master key to the activation of TLR4/MD-2-positive cells. *Eur. J. Immunol. 36*, 701–711.

(11) Patel, D. S., Re, S., Wu, E. L., Qi, Y., Klebba, P. E., Widmalm, G., Yeom, M. S., Sugita, Y., and Im, W. (2016) Dynamics and Interactions of OmpF and LPS: Influence on Pore Accessibility and Ion Permeability. *Biophys. J. 110*, 930–938.

(12) Patel, D. S., Qi, Y., and Im, W. (2017) Modeling and Simulation of Bacterial Outer Membranes and Interactions with Membrane Proteins. *Curr. Opin. Struct. Biol. 43*, 131–140.

(13) Lee, J., Patel, D. S., Kucharska, I., Tamm, L. K., and Im, W. (2017) Refinement of OprH-LPS Interactions by Molecular Simulations. *Biophys. J. 112*, 346–355.

(14) Kim, S., Patel, D. S., Park, S., Slusky, J., Klauda, J. B., Widmalm, G., and Im, W. (2016) Bilayer Properties of Lipid A from Various Gram-Negative Bacteria. *Biophys. J. 111*, 1750–1760.

(15) Guillard, T., Limelette, A., Le Magrex-debar, E., Wynckel, A., Gouali, M., Mariani-Kurkdjian, P., Guyot-Colosio, C., and de Champs, C. (2015) Fatal case of hemolytic-uremic syndrome in an adult due to a rare serogroup O91 Entero hemorrhagic Escherichia coli associated with a Clostridium difficile infection. More than meets the eye. *Int. J. Infect. Dis. 37*, 113–114.

(16) Lundborg, M., Modhukur, V., and Widmalm, G. (2010) Glycosyltransferase functions of E. coli O-antigens. *Glycobiology 20*, 366–368.

(17) Rojas-Macias, M. A., Ståhle, J., Lütteke, T., and Widmalm, G. (2015) Development of the ECODAB into a relational database for Escherichia coli O-antigens and other bacterial polysaccharides. *Glycobiology 25*, 341–347.

(18) Kjellberg, A., Weintraub, A., and Widmalm, G. (1999) Structural Determination and Biosynthetic Studies of the O-Antigenic Polysaccharide from the Enterohemorrhagic Escherichia coli O91 Using. *Biochemistry 38*, 12205–12211.

(19) Lycknert, K., and Widmalm, G. (2004) Dynamics of the Escherichia coli O91 O-Antigen Polysaccharide in Solution as Studied by Carbon-13 NMR Relaxation. *Biomacromolecules 5*, 1015–1020.

(20) Soltesova, M., Kowalewski, J., and Widmalm, G. (2013) Dynamics of exocyclic groups in the Escherichia coli O91 O-antigen polysaccharide in solution studied by carbon-13 NMR relaxation. *J. Biomol. NMR 57*, 37–45.

(21) Vulliez-Le Normand, B., Saul, F. A., Phalipon, A., Bélot, F., Guerreiro, C., Mulard, L. A., and Bentley, G. A. (2008) Structures of synthetic O-antigen fragments from serotype 2a Shigella flexneri in complex with a protective monoclonal antibody. *Proc. Natl. Acad. Sci. U. S. A. 105*, 9976–9981.

(22) Boutet, J., Blasco, P., Guerreiro, C., Thouron, F., Dartevelle, S., Nato, F., Cañada, F. J., Ardá, A., Phalipon, A., Jiménez-Barbero, J., and Mulard, L. A. (2016) Detailed Investigation of the Immunodominant Role of O-Antigen Stoichiometric O-Acetylation as Revealed by Chemical Synthesis , Immunochemistry , Solution Conformation and STD-NMR Spectroscopy for Shigella flexneri 3a. *Chem. Eur. J. 22*, 10892–10911.

(23) Haxaire, K., Braccini, I., Milas, M., Rinaudo, M., and Pérez, S. (2000) Conformational behavior of hyaluronan in relation to its physical properties as probed by molecular modeling. *Glycobiology 10*, 587–594.

(24) Sarkar, A., Fontana, C., Imberty, A., Pérez, S., and Widmalm, G. (2013) Conformational Preferences of the O-Antigen Polysaccharides of Escherichia coli O5ac and O5ab Using NMR Spectroscopy and Molecular Modeling. *Biomacromolecules 14*, 2215–2224.

(25) Pomin, V. H. (2014) NMR-based dynamics of free glycosaminoglycans in solution. *Analyst 139*, 3656–3665.

(26) Sánchez-Medina, I., Frank, M., Lieth, C. Von Der, and Kamerling, J. P. (2009) Conformational analysis of the neutral exopolysaccharide produced by Lactobacillus delbrueckii ssp. bulgaricus LBB.B26. *Org. Biomol. Chem. 7*, 280–287.

(27) Jo, S., Wu, E. L., Stuhlsatz, D., Klauda, J. B., Mackerell Jr, A. D., Widmalm, G., and Im, W. (2015) Lipopolysaccharide Membrane Building and Simulation. *Methods Mol. Biol. 1273*, 391–406.

(28) Khalid, S., Berglund, N. A., Holdbrook, D. A., Leung, Y. M., and Parkin, J. (2015) The membranes of Gram-negative bacteria: progress in molecular modelling and simulation. *Biochem. Soc. Trans. 43*, 162–167.

(29) Galochkina, T., Zlenko, D., Nesterenko, A., Kovalenko, I., Strakhovskaya, M., Averyanov, A., and Rubin, A. (2016) Conformational Dynamics of the Single Lipopolysaccharide O-Antigen in Solution. *ChemPhysChem 17*, 2839–2853.

(30) Findeisen, M., Brand, T., and Berger, S. (2007) A 1H-NMR thermometer suitable for cryoprobes. *Magn. Reson. Chem. 45*, 175–178.

(31) Thrippleton, M. J., and Keeler, J. (2003) Elimination of zero-quantum interference in two-dimensional NMR spectra. *Angew. Chemie - Int. Ed. 42*, 3938–3941.

(32) Wagner, R., and Berger, S. (1997) Heteronuclear Edited Gradient Selected 1D and 2D NOE Spectra: Determination of the NOE Effect between Chemically Equivalent Protons. *Magn. Reson. Chem. 35*, 199–202.

(33) Widmalm, G., Byrd, R. A., and Egan, W. (1992) A conformational study of α-L-Rhap-(1→2)-α-L-Rhap-(1→OMe) by NMR nuclear Overhauser effect spectroscopy (NOESY) and molecular dynamics calculations. *Carbohydr. Res. 229*, 195–211.

(34) Macura, S., Farmer II, B. T., and Brown, L. R. (1986) An Improved Method for the Determination of Cross-Relaxation Rates from NOE Data. *J. Magn. Reson. 70*, 493–499.

(35) Hu, H., and Krishnamurthy, K. (2006) Revisiting the initial rate approximation in kinetic NOE

measurements. *J. Magn. Reson. 182*, 173–177.

(36) Thomas, P. D., Basus, V. J., and James, T. L. (1991) Protein solution structure determination using distances from two-dimensional nuclear Overhauser effect experiments: effect of approximations on the accuracy of derived structures. *Proc. Natl. Acad. Sci. U. S. A. 88*, 1237–1241.

(37) Efron, B., and Stein, C. (1981) The Jackknife estimate of variance. *Ann. Stat. 9*, 586–596.

(38) Säwén, E., Massad, T., Landersjö, C., Damberg, P., and Widmalm, G. (2010) Population distribution of flexible molecules from maximum entropy analysis using different priors as background information: application to the Φ,Ψ-conformational space of the α-(1→2)-linked mannose disaccharide present in N- and O-linked glycoprotein. *Org. Biomol. Chem. 8*, 3684–3695.

(39) Guvench, O., Hatcher, E. R., Venable, R. M., Pastor, R. W., and Mackerell Jr, A. D. (2009) CHARMM Additive All-Atom Force Field for Glycosidic Linkages between Hexopyranoses. *J. Chem. Theory Comput. 5*, 2353–2370.

(40) Guvench, O., Mallajosyula, S. S., Raman, E. P., Hatcher, E., Vanommeslaeghe, K., Foster, T. J., Jamison II, F. W., and Mackerell Jr, A. D. (2011) CHARMM Additive All-Atom Force Field for Carbohydrate Derivatives and Its Utility in Polysaccharide and Carbohydrate-Protein Modeling. *J. Chem. Theory Comput. 7*, 3162–3180.

(41) Guvench, O., Greene, S. N., Kamath, G., Brady, J. W., Venable, R. M., Pastor, R. W., and Mackerell Jr, A. D. (2008) Additive Empirical Force Field for Hexopyranose Monosaccharides. *J. Comput. Chem. 29*, 2543–2564.

(42) Patel, D. S., Pendrill, R., Mallajosyula, S. S., Widmalm, G., and Mackerell Jr, A. D. (2014) Conformational Properties of α- or β-(1→6)-Linked Oligosaccharides: Hamiltonian Replica Exchange MD Simulations and NMR Experiments. *J. Phys. Chem. B 118*, 2815–2871.

(43) Jo, S., Kim, T., Iyer, V. G., and Im, W. (2008) CHARMM-GUI: A Web-Based Graphical User Interface for CHARMM. *J. Comput. Chem. 29*, 1859–1865.

(44) Jo, S., Song, K. C., Desaire, H., MacKerell Jr, A. D., and Im, W. (2011) Glycan reader: Automated sugar identification and simulation preparation for carbohydrates and glycoproteins. *J. Comput. Chem. 32*, 3135–3141.

(45) Brooks, B. R., Brooks III, C. L., Mackerell Jr., A. D., Nilsson, L., Petrella, R. J., Roux, B., Won, Y., Archontis, G., Bartels, C., Boresch, S., Caflisch, A., Caves, L., Cui, Q., Dinner, A. R., Feig, M., Fischer, S., Gao, J., Hodoscek, M., Im, W., Kuczera, K., Lazaridis, T., Ma, J., Ovchinnikov, V., Paci, E., Pastor, R. W., Post, C. B., Pu, J. Z., Schaefer, M., Tidor, B., Venable, R. M., Woodcock, H. L., Wu, X., Yang, W., York, D. M., and Karplus, M. (2009) CHARMM. *J. Comput. Chem. 30*, 1545–1614.

(46) Wu, E. L., Engström, O., Jo, S., Stuhlsatz, D., Yeom, M. S., Klauda, J. B., Widmalm, G., and Im, W. (2013) Molecular dynamics and NMR spectroscopy studies of E. coli lipopolysaccharide structure and dynamics. *Biophys. J. 105*, 1444–1455.

(47) Wu, E. L., Fleming, P. J., Yeom, M. S., Widmalm, G., Klauda, J. B., Fleming, K. G., and Im, W. (2014) E. coli outer membrane and interactions with OmpLA. *Biophys. J. 106*, 2493–2502.

(48) Jo, S., Kim, T., and Im, W. (2007) Automated builder and database of protein/membrane complexes for molecular dynamics simulations. *PLoS One 2*, e880.

(49) Jo, S., Lim, J. B., Klauda, J. B., and Im, W. (2009) CHARMM-GUI membrane builder for

mixed bilayers and its application to yeast membranes. *Biophys. J. 97*, 50–58.

(50) Wu, E. L., Cheng, X., Jo, S., Rui, H., Song, K. C., Dávila-Contreras, E. M., Qi, Y., Lee, J., Monje-Galvan, V., Venable, R. M., Klauda, J. B., and Im, W. (2014) CHARMM-GUI membrane builder toward realistic biological membrane simulations. *J. Comput. Chem. 35*, 1997–2004.

(51) Hoover, W. G. (1985) Canonical dynamics: Equilibrium phase-space distributions. *Phys. Rev. A 31*, 1695–1697.

(52) Andersen, H. C. (1980) Molecular dynamics simulations at constant pressure and/or temperature. *J. Chem. Phys. 72*, 2384–2393.

(53) Nosé, S., and Klein, M. L. (1983) A study of solid and liquid carbon tetrafluoride using the constant pressure molecular dynamics technique. *J. Chem. Phys. 78*, 6928–6939.

(54) Phillips, J. C., Braun, R., Wang, W., Gumbart, J., Tajkhorshid, E., Villa, E., Chipot, C., Skeel, R. D., Kalé, L., and Schulten, K. (2005) Scalable molecular dynamics with NAMD. *J. Comput. Chem. 26*, 1781–1802.

(55) Lee, J., Cheng, X., Swails, J. M., Yeom, M. S., Eastman, P. K., Lemkul, J. A., Wei, S., Buckner, J., Jeong, J. C., Qi, Y., Jo, S., Pande, V. S., Case, D. A., Brooks, C. L., MacKerell, A. D., Klauda, J. B., and Im, W. (2016) CHARMM-GUI Input Generator for NAMD, GROMACS, AMBER, OpenMM, and CHARMM/OpenMM Simulations Using the CHARMM36 Additive Force Field. *J. Chem. Theory Comput. 12*, 405–413.

(56) Feller, S. E., Zhang, Y., Pastor, R. W., and Brooks, B. R. (1995) Constant pressure molecular dynamics simulation: The Langevin piston method. *J. Chem. Phys. 103*, 4613–4621.

(57) Martyna, G. J., Tobias, D. J., and Klein, M. L. (1994) Constant pressure molecular dynamics algorithms. *J. Chem. Phys. 101*, 4177–4189.

(58) Ryckaert, J. P., Ciccotti, G., and Berendsen, H. J. C. (1977) Numerical integration of the cartesian equations of motion of a system with constraints: molecular dynamics of n-alkanes. *J. Comput. Phys. 23*, 327–341.

(59) Steinbach, P. J., and Brooks, B. R. (1994) New spherical-cutoff methods for long-range forces in macromolecular simulation. *J. Comput. Chem. 15*, 667–683.

(60) Essmann, U., Perera, L., Berkowitz, M. L., Darden, T., Lee, H., and Pedersen, L. G. (1995) A smooth particle mesh Ewald method. *J Chem Phys 103*, 8577–8593.

(61) Klauda, J. B., Venable, R. M., Freites, J. A., O'Connor, J. W., Tobias, D. J., Mondragon-Ramirez, C., Vorobyov, I., MacKerell Jr., A. D., and Richard W. Pastor. (2010) Update of the CHARMM all-atom additive force field for lipids: Validation on Six lipid types. *J. Phys. Chem. B 114*, 7830–7843.

(62) Jorgensen, W. L., Chandrasekhar, J., Madura, J. D., Impey, R. W., and Klein, M. L. (1983) Comparison of simple potential functions for simulating liquid water. *J. Chem. Phys. 79*, 926–935.

(63) Kjellberg, A., Rundlöf, T., Kowalewski, J., and Widmalm, G. (1998) Motional properties of two vicinally disubstituted trisaccharides as studied by multiple-field carbon-13 NMR relaxation. *J. Phys. Chem. B 102*, 1013–1020.

(64) Kowalewski, J., and Mäler, L. (2006) Nuclear Spin Relaxation in Liquids: Theory, Experiments, and Applications. *Nucl. Spin Relax. Liq. Theory, Exp. Appl.* CRC Press, Taylor & Francis, New York, NY.

(65) Lipari, G., and Szabo, A. (1982) Model-free approach to the interpretation of nuclear magnetic resonance relaxation in macromolecules. 1. Theory and range of validity. *J. Am. Chem. Soc. 104*, 4546–4559.

(66) Dixon, A. M., Venable, R., Widmalm, G., Bull, T. E., and Pastor, R. W. (2003) Application of NMR, molecular simulation, and hydrodynamics to conformational analysis of trisaccharides. *Biopolymers 69*, 448–460.

(67) Landersjö, C., and Widmalm, G. (2002) Solution structure of a pentasaccharide representing the repeating unit of the O-antigen polysaccharide from Escherichia coli O142: NMR spectroscopy and molecular simulation studies. *Biopolymers 64*, 283–291.

(68) Stenutz, R., Carmichael, I., Widmalm, G., and Serianni, A. S. (2002) Hydroxymethyl Group Conformation in Saccharides: Structural Dependencies of 2JHH, 3JHH, and 1JCH Spin−Spin Coupling Constants. *J. Org. Chem. 67*, 949–958.

(69) Pendrill, R., Säwen, E., and Widmalm, G. (2013) Conformation and Dynamics at a Flexible Glycosidic Linkage Revealed by NMR Spectroscopy and Molecular Dynamics Simulations: Analysis of β-L-Fucp-(1→6)-α-D-Glcp-OMe in Water Solution. *J. Phys. Chem. B 117*, 14709–14722.

(70) Fontana, C., Kovacs, H., and Widmalm, G. (2014) NMR structure analysis of uniformly 13C-labeled carbohydrates. *J. Biomol. NMR 59*, 95–110.

(71) Gitti, R., Long, G., and Bush, C. A. (1994) Measurement of long-range2 13-1H coupling constants of 95% uniformly 13C-labeled polysaccharide from Streptococcus mitis J22. *Biopolymers 34*, 1327–1338.

(72) Xu, Q., Mohan, S., and Bush, C. A. (1996) A flexible model for the cell wall polysaccharide of Streptococcus mitis J22 determined by three-dimensional 13C edited nuclear Overhauser effect spectroscopy and 13C-1H long-range coupling constants combined with molecular modeling. *Biopolymers 38*, 339–353.

(73) Xu, Q., and Bush, C. A. (1996) Molecular modeling of the flexible cell wall polysaccharide of Streptococcus mitis J22 on the basis of heteronuclear NMR coupling constants. *Biochemistry 35*, 14521–14529.

(74) Eklund, R., Lycknert, K., Söderman, P., and Widmalm, G. (2005) A conformational dynamics study of α-L-Rhap-(1→2)[α-L-Rhap-(1→3)]-α-L-Rhap-OMe in solution by NMR experiments and molecular simulations. *J. Phys. Chem. B 109*, 19936–19945.

(75) Jonsson, K. H. M., Pendrill, R., and Widmalm, G. (2011) NMR analysis of conformationally dependent (n)J(C,H) and (n)J(C,C) in the trisaccharide α-L-Rhap-(1 → 2)[α-L-Rhap-(1 → 3)]-α-L-Rhap-OMe and a site-specifically labeled isotopologue thereof. *Magn. Reson. Chem. 49*, 117–24.

(76) Zaccheus, M. V., Pendrill, R., Jackson, T. A., Wang, A., Auzanneau, F.-I., and Widmalm, G. (2012) Conformational Dynamics of a Central Trisaccharide Fragment of the LeaLex Tumor Associated Antigen Studied by NMR Spectroscopy and Molecular Dynamics Simulations. *European J. Org. Chem.* 4705–4715.

(77) Meissner, A., and Sørensen, O. W. (2001) Measurement of J(H,H) and long-range J(X,H) coupling constants in small molecules. Broadband XLOC and J-HMBC. *Magn. Reson. Chem. 39*, 49–52.

(78) Pendrill, R., Sørensen, O. W., and Widmalm, G. (2014) Suppressing one-bond homonuclear

13C,13C scalar couplings in the J-HMBC NMR experiment: application to 13C site-specifically labeled oligosaccharides. *Magn. Reson. Chem. 52*, 82–86.

(79) Lycknert, K., Edebrink, P., and Widmalm, G. (2004) A Conformational Carbohydrate Scaffold is Present in the Short-Chain Lipopolysaccharides ofMoraxella catarrhalis. *Angew. Chemie Int. Ed. 43*, 2288–2290.

(80) Battistel, M. D., Pendrill, R., Widmalm, G., and Freedberg, D. I. (2013) Direct Evidence for Hydrogen Bonding in Glycans: A Combined NMR and Molecular Dynamics Study. *J. Phys. Chem. B 117*, 4850–4859.

(81) Jo, S., and Im, W. (2013) Glycan fragment database: A database of PDB-based glycan 3D structures. *Nucleic Acids Res. 41*, D470–D474.

(82) Feller, S. E., Pastor, R. W., Rojnuckarin, A., Bogusz, S., and Brooks, B. R. (1996) Effect of electrostatic force truncation on interfacial and transport properties of water. *J. Phys. Chem. 100*, 17011–17020.

(83) Mills, R. (1973) Self-diffusion in normal and heavy water in the range 1-45.deg. *J. Phys. Chem. 77*, 685–688.

(84) Lins, R. D., and Straatsma, T. P. (2001) Computer Simulation of the Rough Lipopolysaccharide Membrane of Pseudomonas aeruginosa. *Biophys. J. 81*, 1037–1046.

(85) Vaara, M. (1992) Agents that increase the permeability of the outer membrane. *Microbiol. Rev. 56*, 395–411.

(86) Schneck, E., Schubert, T., Konovalov, O. V, Quinn, B. E., Gutsmann, T., Brandenburg, K., Oliveira, R. G., Pink, D. a, and Tanaka, M. (2010) Quantitative determination of ion distributions in bacterial lipopolysaccharide membranes by grazing-incidence X-ray fluorescence. *Proc. Natl. Acad. Sci. U. S. A. 107*, 9147–51.

(87) Neu, H. C., Ashman, D. F., and Price, T. D. (1967) Effect of Ethylenediaminetetraacetic Acid-Tris (hydroxymethyl) aminomethane on Release of the Acid-soluble Nucleotide Pool and on Break-down of Ribosomal Ribonucleic Acid in Escherichia coli. *J. Bacteriol. 93*, 1360–1368.

Tables

Table 1. Inter- and intraresidue proton-proton cross-relaxation rates (σ in s^{-1}) in the *E. coli* O91 PS derived from NOE buildup curves analyzed by the PANIC approach. Experimentally derived distances (r_{NMR} in Å) are given together with calculated averaged proton-proton distances ($r_{Solution}$, r_{LPS5}, r_{LPS10} in Å) from the solution, LPS5 and LPS10 MD simulations.

Proton pair	σ_{NMR}	r_{NMR}	$r_{Solution}$	r_{LPS5}	r_{LPS10}
E1-A4	1.47±0.05 0.74±0.004[a]	2.60±0.02 2.58±0.001[a]	2.195±0.001	2.200±0.02	2.197±0.01
E1-A6$_{pro-S}$	1.49±0.02 0.62±0.003[a]	2.59±0.04 2.66±0.001[a]	2.723±0.02	2.697±0.06	2.717±0.04
A1-D4	1.19±0.08	2.69±0.01	2.301±0.01	2.382±0.09	2.432±0.04
D1-B4	1.74±0.13	2.52±0.01	2.361±0.01	2.559±0.22	2.595±0.04
D1-B5	0.40±0.003	3.21±0.06	3.871±0.05	3.394±0.22	3.355±0.02
B1-C3	1.37±0.08	2.63±0.0003	2.280±0.01	2.286±0.02	2.277±0.001
C1-E4	2.10[b]	2.44	2.429±0.01	2.607±0.14	2.601±0.06
C1-E5	0.50±0.06	3.10±0.07	3.185±0.02	3.475±0.14	3.509±0.10
E1-E2	2.38±0.14 1.17±0.008[a]	2.39[c]	2.394±0.002	2.396±0.001	2.398±0.01
A1-A3	2.18±0.07	2.43±0.02	2.461±0.001	2.454±0.001	2.454±0.001
D1-D3	1.40±0.07	2.62±0.01	2.515±0.006	2.509±0.001	2.506±0.001
D1-D5	1.70±0.10	2.53±0.002	2.400±0.001	2.395±0.003	2.395±0.001
B1-B3	1.21±0.01	2.68±0.04	2.477±0.001	2.468±0.004	2.468±0.001
B1-B5	1.58±0.07	2.56±0.01	2.408±0.001	2.406±0.002	2.406±0.001

[a] From a 1D ^{1}H,^{1}H-NOESY spectrum of the natural abundance PS.

[b] Deduced from the C1-E4/C5 interactions with $\sigma = 4.51\pm0.08$ s^{-1}; see text for details.

[c] Reference distance from the MD simulations.

Table 2. Transglycosidic coupling constants ($^3J_{CH}$ in Hz) related to ψ_H torsion angles obtained from ^{1}H,^{1}H-NOESY spectra of [1-^{13}C]-labeled *E. coli* O91 PS and from the solution, LPS5 and LPS10 MD simulations based on quadrant distributions.

Linkage	Region	NMR	Solution	LPS5	LPS10
E-A	Q1		1.12	2.04	2.25
	Q2		-	-	-
	Q3		3.08	4.07	3.43
	Q4		5.26	5.27	5.23
	Q4$^{(syn+)}$		4.67	4.76	4.71
	Q4$^{(syn-)}$		5.85	5.78	5.79
	Q1-Q4	5.2	5.26 (0.03)[a]	5.22 (0.06)	5.21 (0.06)
A-D	Q1		6.13	6.09	6.11
	Q2		5.66	5.48	5.50
	Q3		6.58	6.64	6.70
	Q4		7.38	7.00	7.29
	Q1-Q4	5.3	5.74 (0.02)	5.77 (0.17)	5.86 (0.06)
D-B	Q1		5.94	3.78	5.99
	Q2		5.64	5.37	5.27
	Q3		6.91	6.87	6.86
	Q4		7.48	7.37	7.38
	Q1-Q4	n.d.[b]	5.75 (0.02)	6.01 (0.34)	6.04 (0.03)
B-C	Q1		-	7.33	4.94
	Q2		6.30	6.49	6.17
	Q3		5.83	5.75	5.74
	Q4		6.08	6.07	6.07
	Q1-Q4	n.d.	5.84 (0.08)	5.80 (0.06)	5.75 (0.01)
C-E	Q1		5.51	5.43	2.66
	Q2		5.84	5.73	5.72
	Q3		6.83	6.84	6.81
	Q4		7.49	7.35	7.25
	Q1-Q4	5.9	5.97 (0.06)	6.32 (0.20)	6.24 (0.04)

[a] Standard errors of the three replicas from the MD simulations are shown in parentheses.
[b] n.d. = not determined.

Table 3. ^{13}C NMR relaxation and model-free dynamical parameters for the *E. coli* O91 PS.

MF and NMR parameters	Sugar residues				
	E	A	D	B	C
S^2	0.50 (0.03)[b]	0.53 (0.02)	0.47 (0.03)	0.48 (0.03)	0.46 (0.03)
S^2[NMR]	0.62	0.63	0.64	0.64	0.62
τ_e /ps	355 (34)	298 (22)	182 (28)	202 (32)	304 (33)
τ_e /ps (scaled)[a]	343	181	172	204	325
τ_e[NMR] /ps	517	387	366	376	455
τ_M /ns	5.72 (1.16)	8.94 (1.04)	5.79 (1.19)	5.42 (1.13)	5.16 (1.08)
$<T_1>$ @ 9.4 T /ms	312 (3)	405 (29)	357 (9)	356 (39)	335 (33)
T_1[NMR] @ 9.4 T /ms	288	315	332	327	302
$<T_1>$ @ 14.1 T /ms	515 (28)	654 (22)	586 (44)	593 (30)	497 (15)
T_1[NMR] @ 14.1 T /ms	461	484	507	503	467

[a] Scaling factor: τ_M^{NMR}/τ_M^{MD}. [b] The error is given as one standard deviation.

Figures
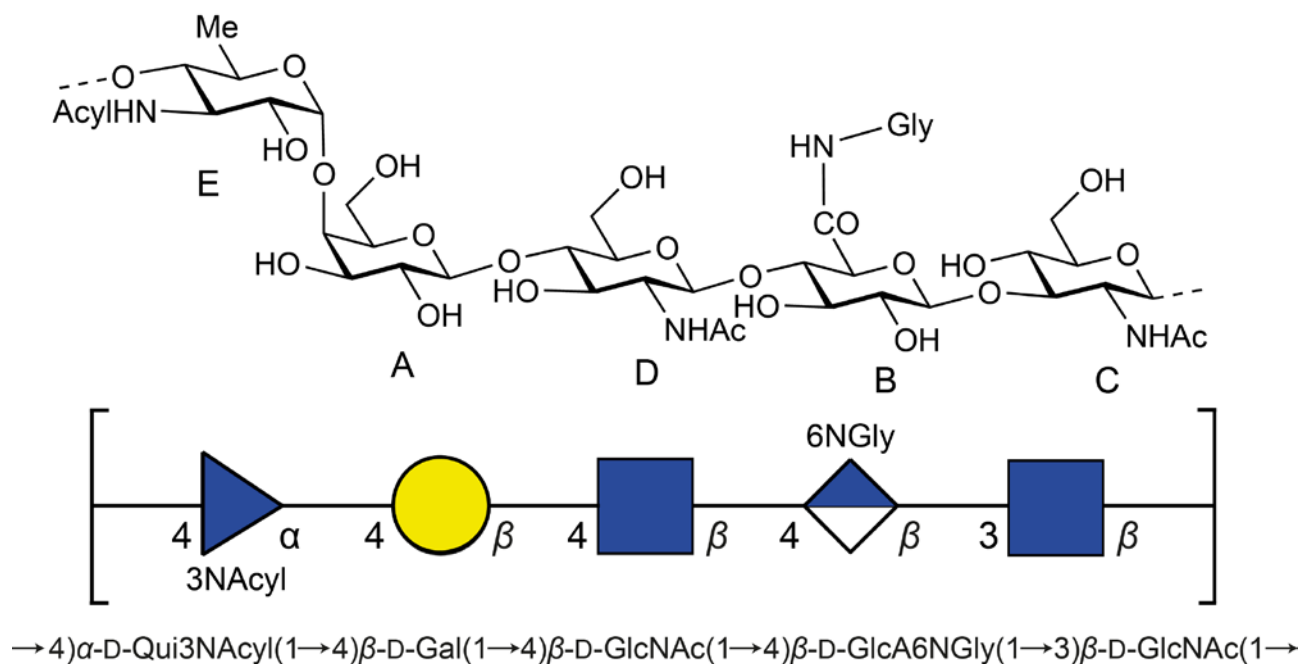
Figure 1. Schematic structure of the repeating unit of the O-antigen polysaccharide (PS) from *E. coli* O91 with sugar residues annotated as A – E (top), in symbol nomenclature for glycans (SNFG) and IUPAC/IUBMB text representation (bottom).
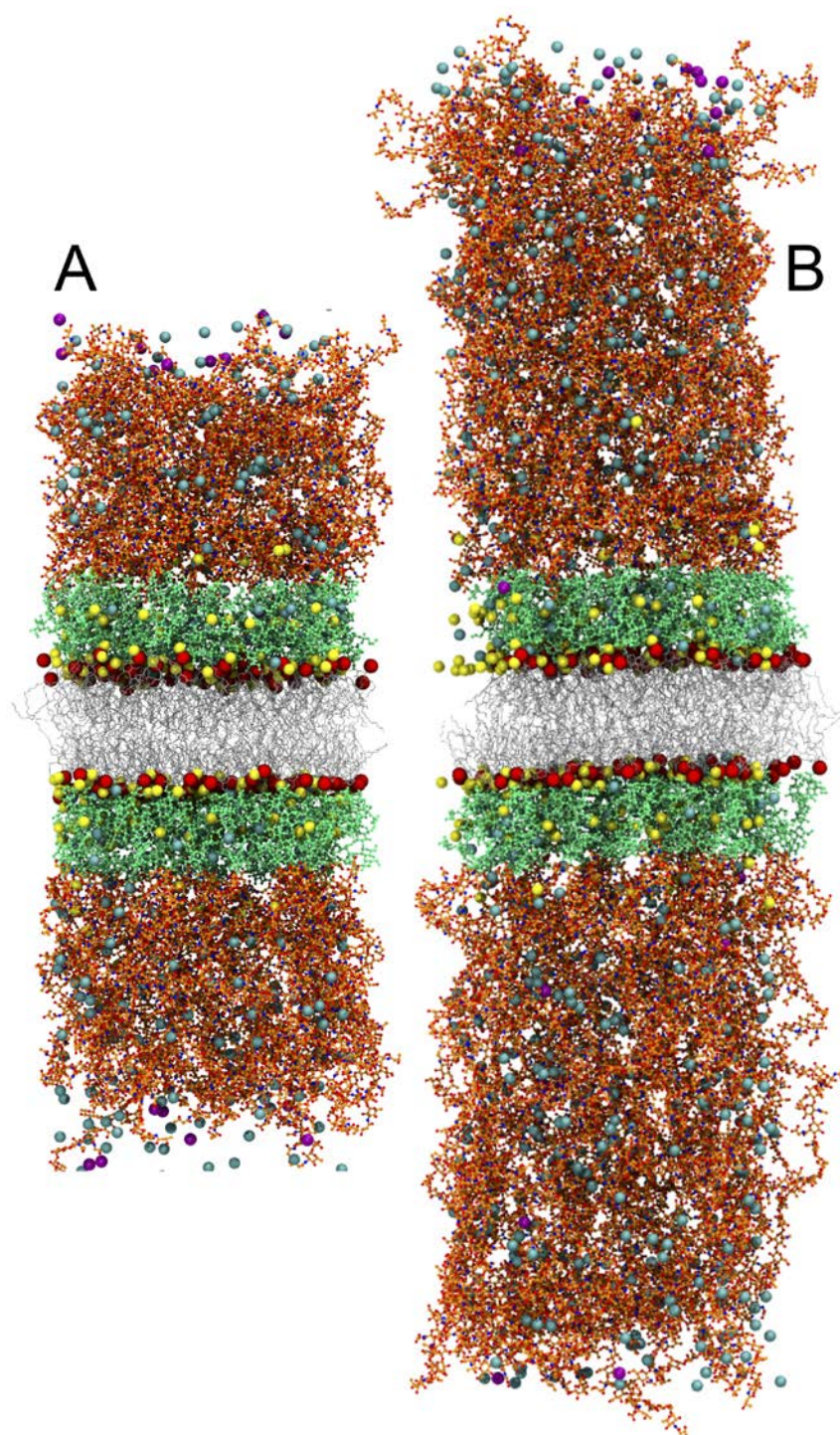
Figure 2. LPS5 and LPS10 lipid bilayer snapshots from the 400-ns time point: (A) LPS5 (lipid A + R1 core + 5 units of O91 antigen) and (B) LPS10 (lipid A + R1 core + 10 units of O91 antigen). Lipid A in gray, R1 core in green, and O91 antigen repeating units are orange-colored. Phosphate groups in red color and calcium, potassium and chloride ions are shown in yellow-, cyan- and purple-colored spheres. Water molecules are not shown for clarity.
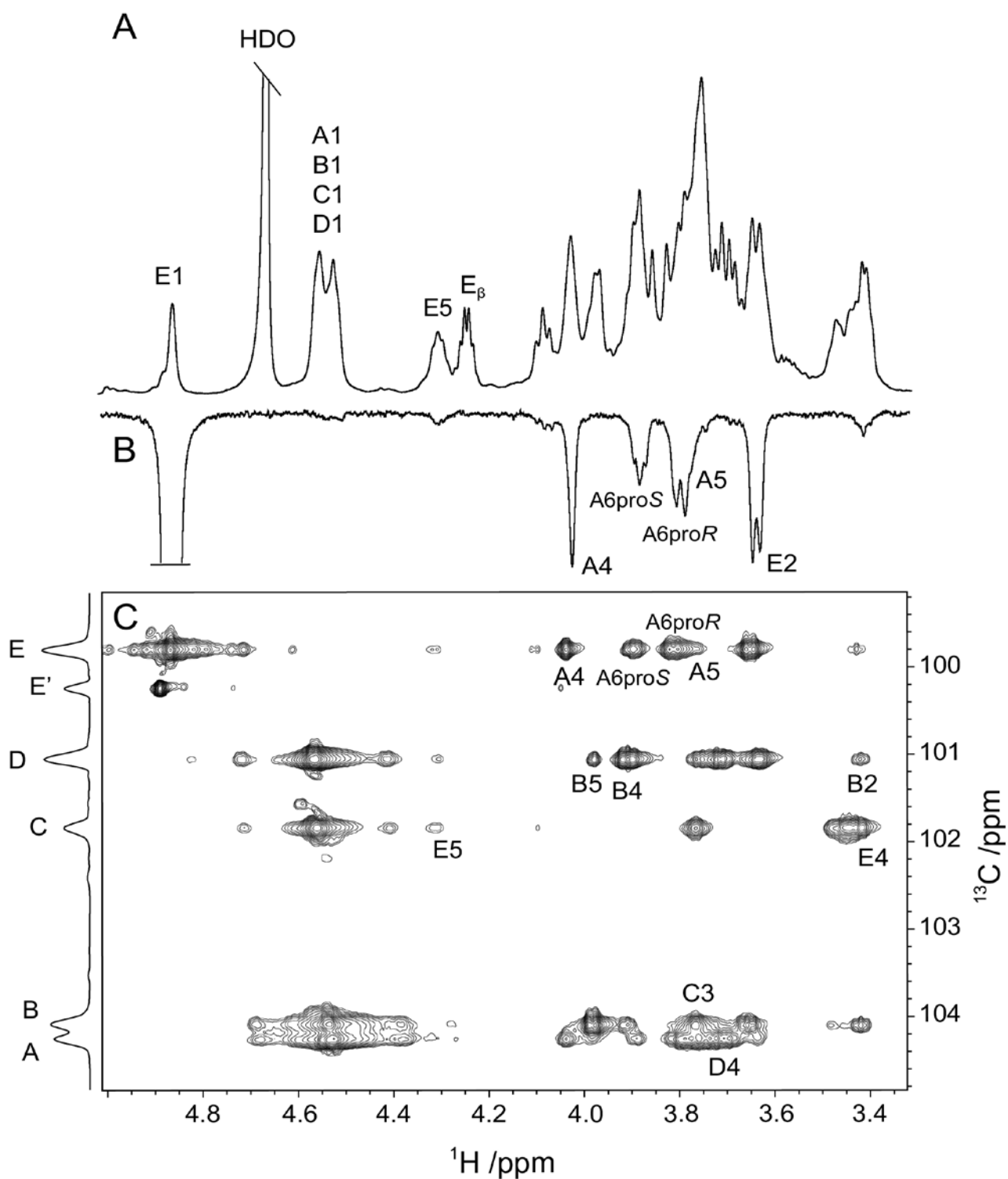
Figure 3. Part of a ^{1}H NMR spectrum of *E. coli* O91 PS (natural abundance) (A) and a 1D ^{1}H,^{1}H-NOESY spectrum of the same material acquired with a mixing time of 160 ms (B). Selected region of a ^{1}H,^{13}C-HSQC-NOESY spectrum (mixing time 40 ms) of [1-^{13}C]-labeled *E. coli* O91 PS (C). Pertinent cross-peaks are annotated.
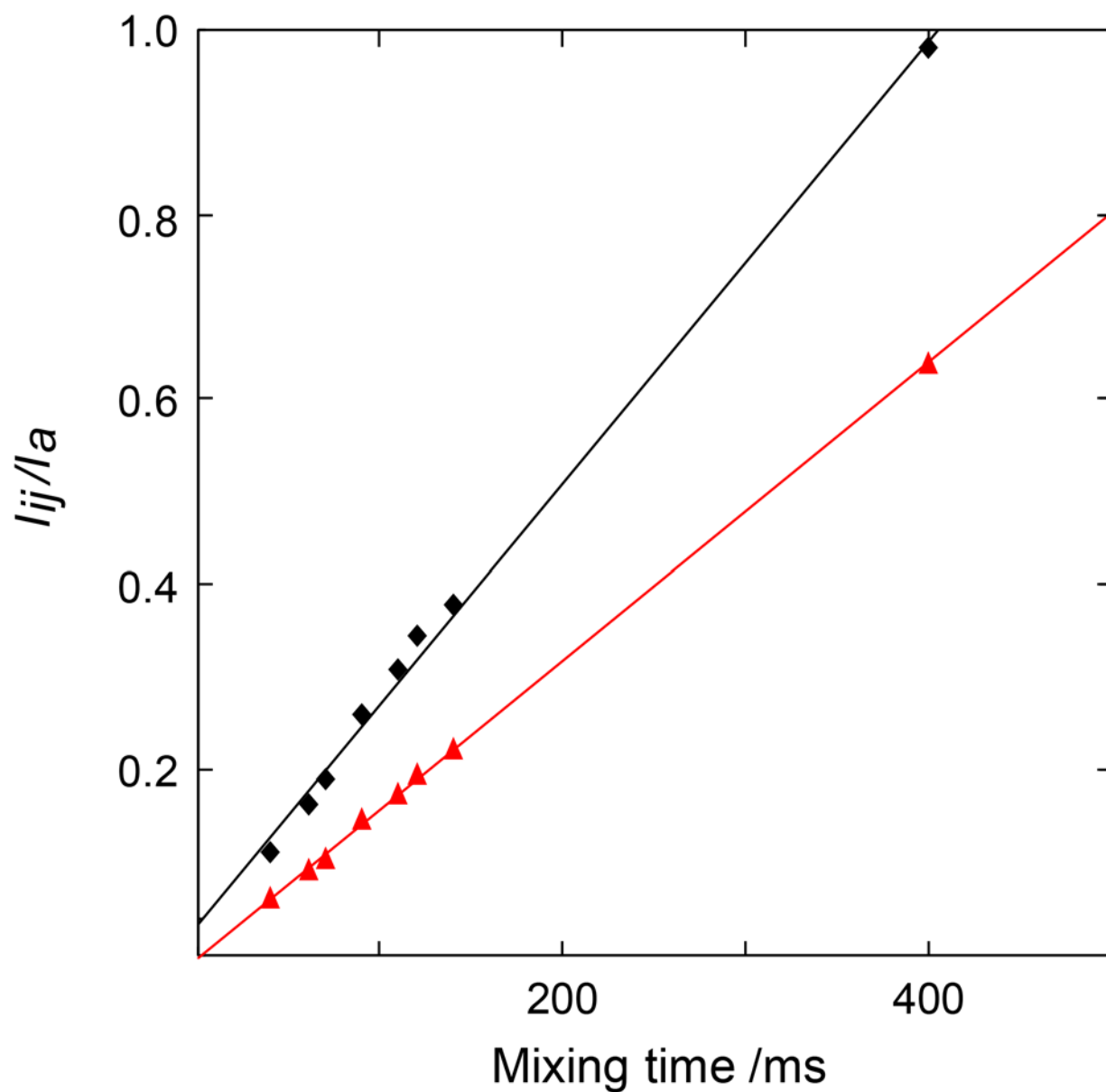
Figure 4. NOE buildup curves obtained from ^{1}H,^{13}C-HSQC-NOESY spectra of [1-^{13}C]-labeled *E. coli* O91 PS and analyzed by the PANIC approach for the proton pairs E1-E2 (black diamonds) and E1-A4 (red triangles); the coefficients of determination $R^2 > 0.995$.
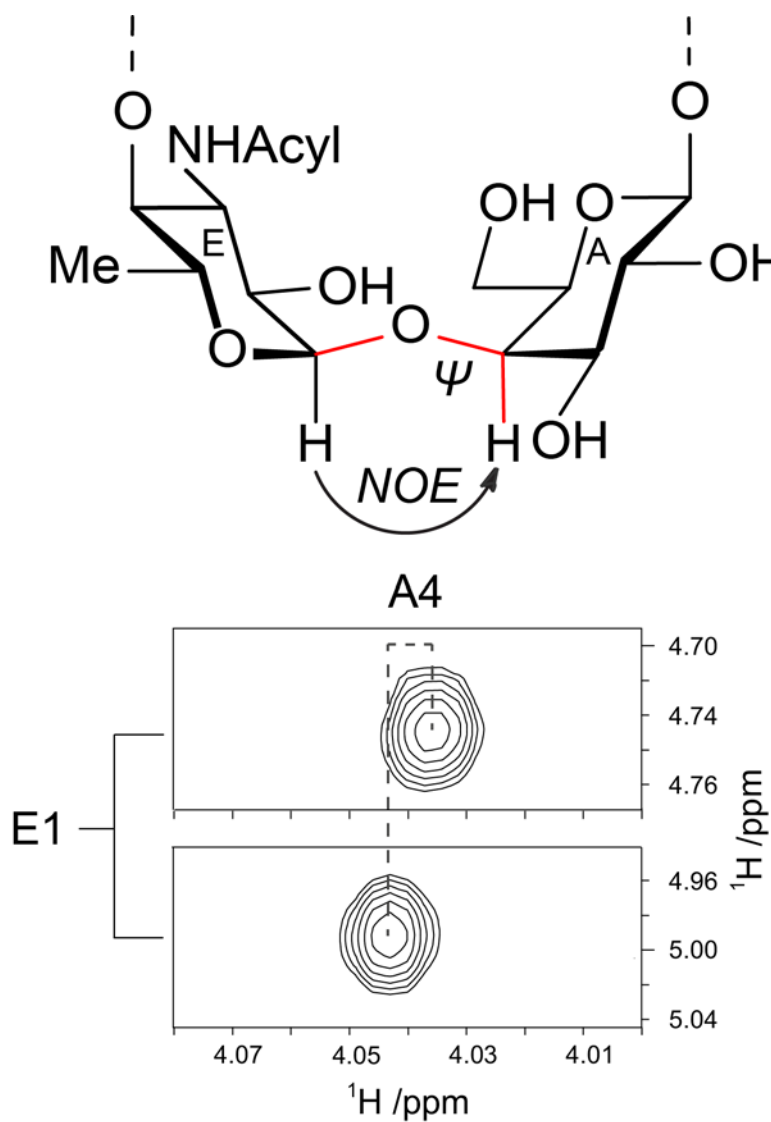
Figure 5. Part of a ^{1}H,^{1}H-NOESY spectrum of [1-^{13}C]-labeled *E. coli* O91 PS acquired with a mixing time of 40 ms where the panels show the E1-A4 NOE cross-peak split in the F_1 dimension due to $^1J_{CH}$ of the anomeric carbon of residue E and the displacement in the F_2 dimension due to $^3J_{CH}$ to the same carbon-13 atom (bottom); schematic representation of the E-A glycosidic linkage region showing the NOE correlation from proton E1 to proton A4; the $^3J_{CH}$ spin-spin coupling pathway, related to the ψ_H torsional angle, is highlighted in red color (top); cf. also Figure 9.
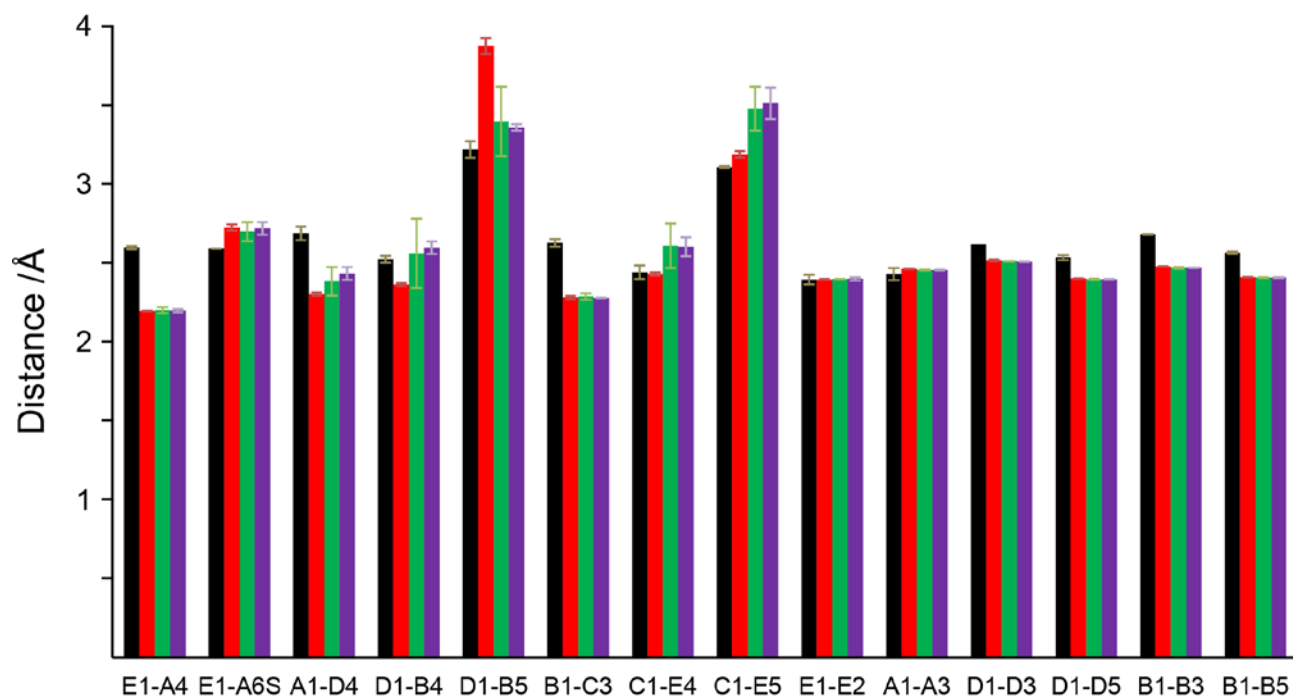
Figure 6. Bar diagram displaying proton-proton distances in *E. coli* O91 PS from NMR (black), including error bar estimates (SEM) based on cross-relaxation rates, and from MD simulations (solution, LPS5 and LPS10 detailed in red, green and purple, respectively).
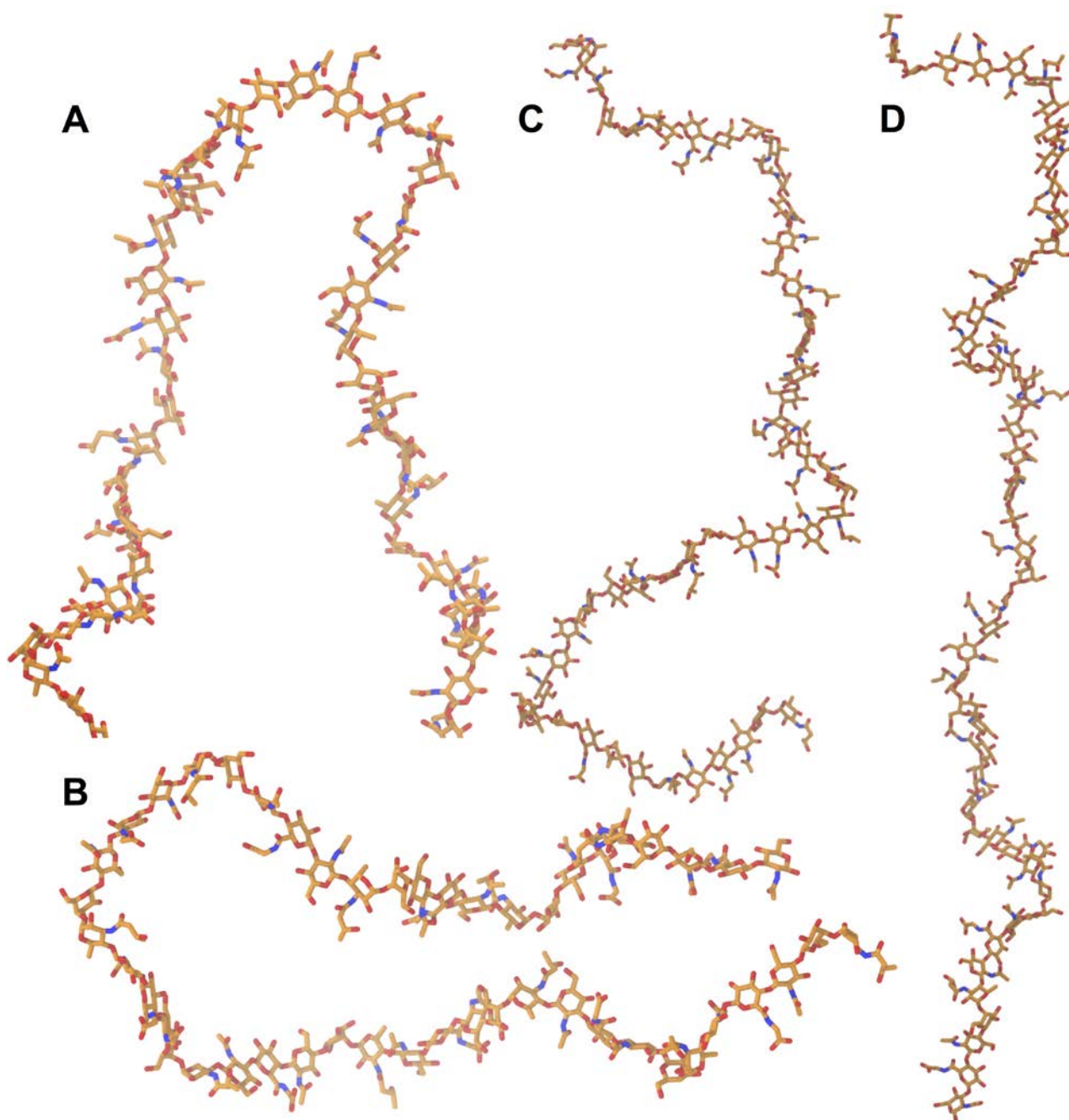
Figure 7. Structures of curved (A and B) and extended (C and D) *E. coli* O91 O-antigen PS molecules randomly selected from the PS-only solution simulations.
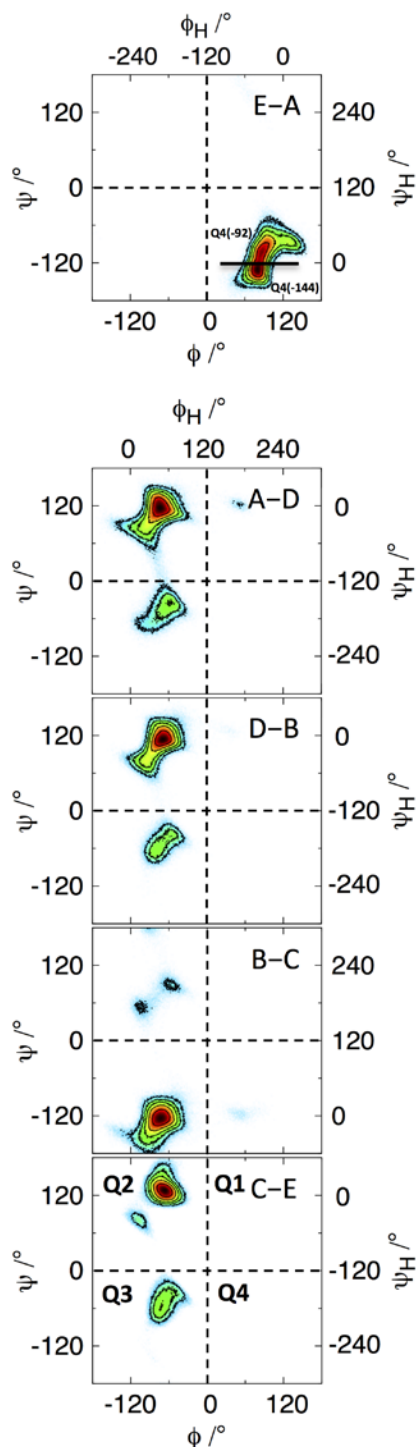
Figure 8. Two-dimensional free energy surfaces of the glycosidic torsion angles ϕ and ψ in the *E. coli* O91 O-antigen from the PS10 MD simulation. Free energies are calculated from the natural logarithm of the relative probability and are given as black = 0, red = 0.5, yellow = 1.0, green = 1.75 and blue = 2.5 kcal·mol^{-1}. The following glycosidic torsion angle definitions are adopted: $\phi =$ O5'-C1'-On-Cn, $\psi =$ C1'-On-Cn-C(n-1), $\phi_H =$ H1'-C1'-On-Cn and $\psi_H =$ C1'-On-Cn-Hn, where n is the linkage position. For the E-A linkage the most highly populated conformations in Q4 occur at $\psi = -92°$ and at $\psi = -144°$.
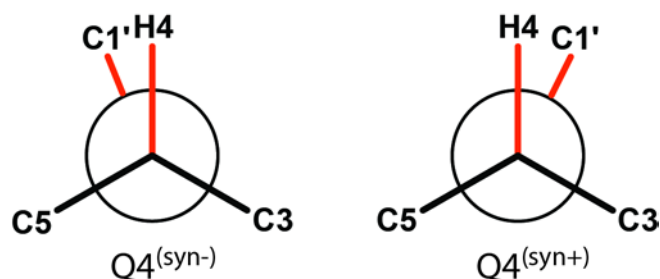
Figure 9. Newman projections of the ψ_H torsion angle related to the $Q4^{(syn-)}$ and $Q4^{(syn+)}$ states of the E-A glycosidic linkage; cf. Figure 5 for the torsion angle of the disaccharide structural element and Figure 8 (top panel) for the population distribution at the glycosidic linkage. Note that in the Newman projection regular atom labeling has been used with atoms from the A residue in front and the anomeric carbon, denoted C1', of residue E in the back.
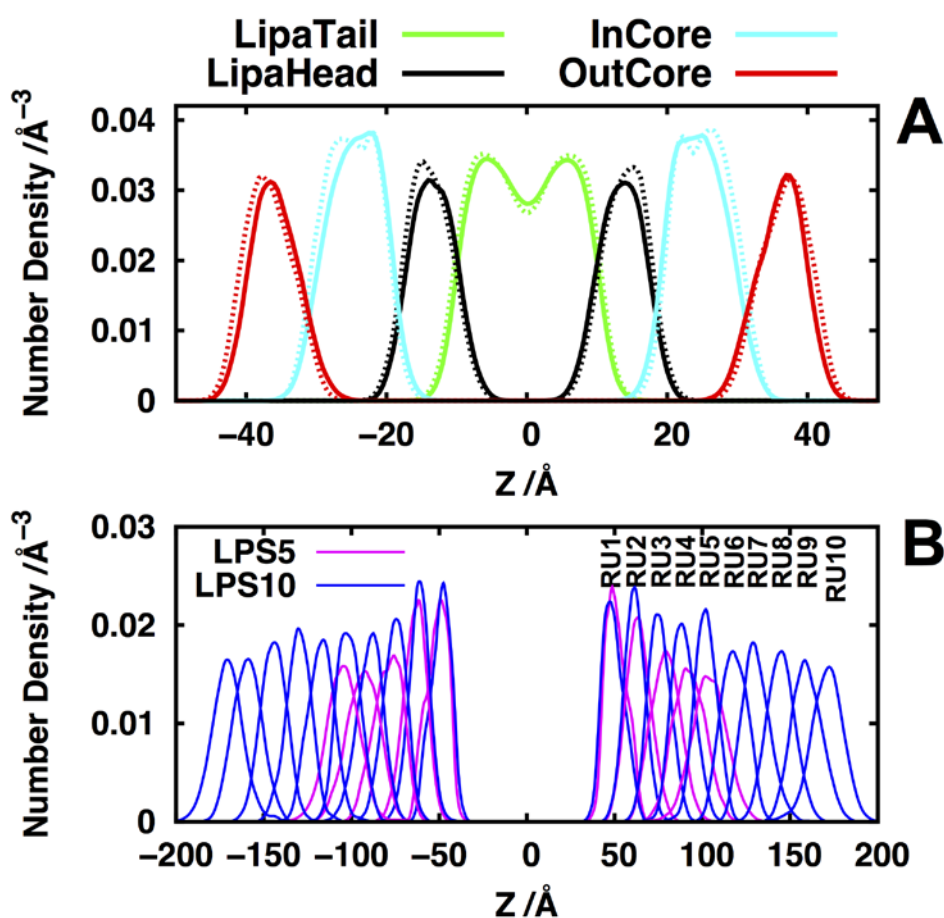

Figure 10. Heavy atoms density profiles along the Z-axis for (A) lipid A acyl chains (LipaTail), lipid A head groups (Head), inner core sugars (InnerCore), and outer core sugars (OuterCore) and (B) O-antigen repeating units RU1 – RU5 in the LPS5 and RU1 – RU10 in the LPS10 bilayers. In (A), solid and dotted lines correspond to LPS10 and LPS5 bilayers in *E. coli* O91.
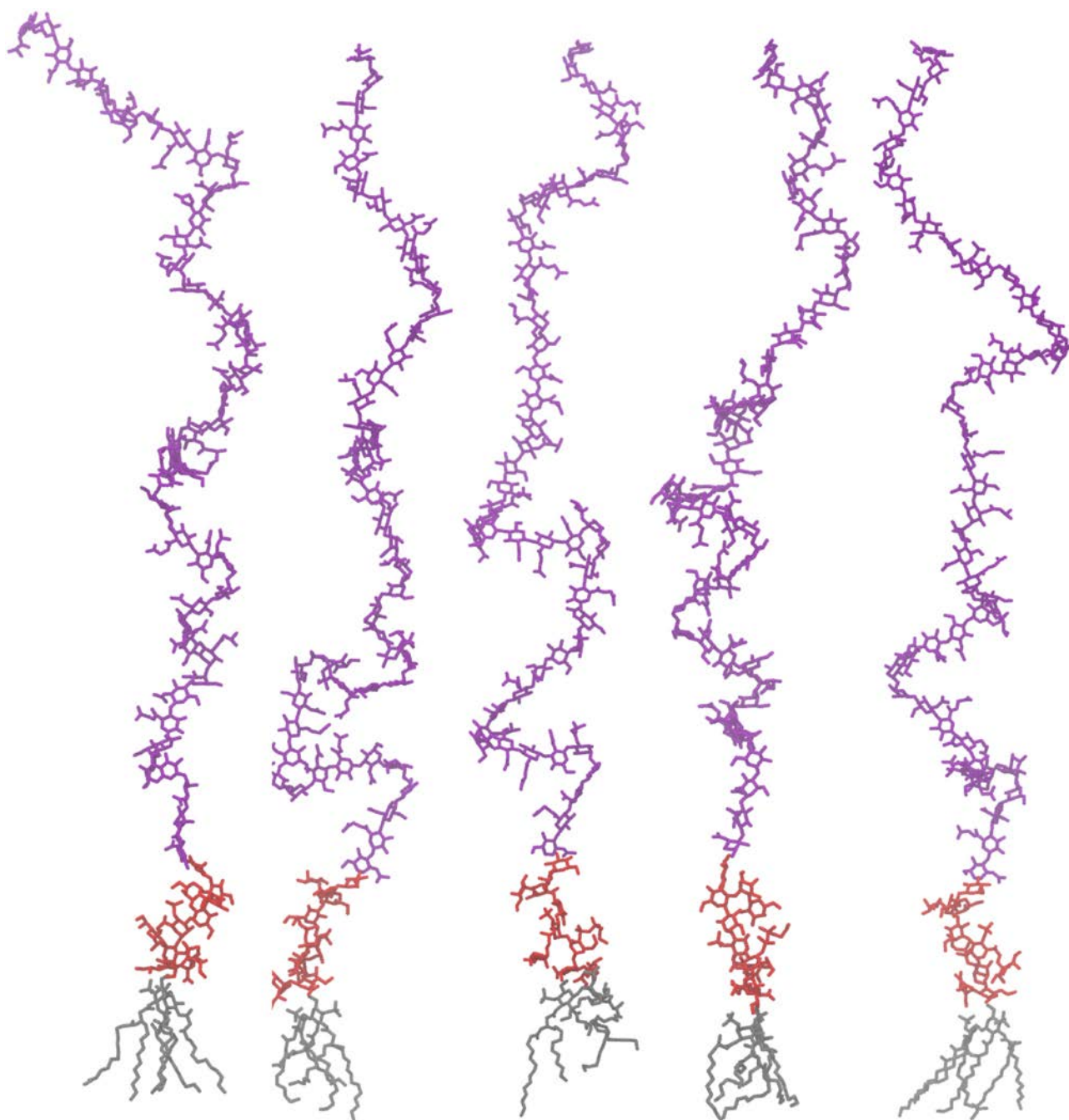
Figure 11. Structures of five randomly selected different *E. coli* O91 LPS10 molecules from the LPS10 bilayer at 400 ns. Lipid A, core sugars, and O-antigen are shown in gray, red, and purple, respectively.
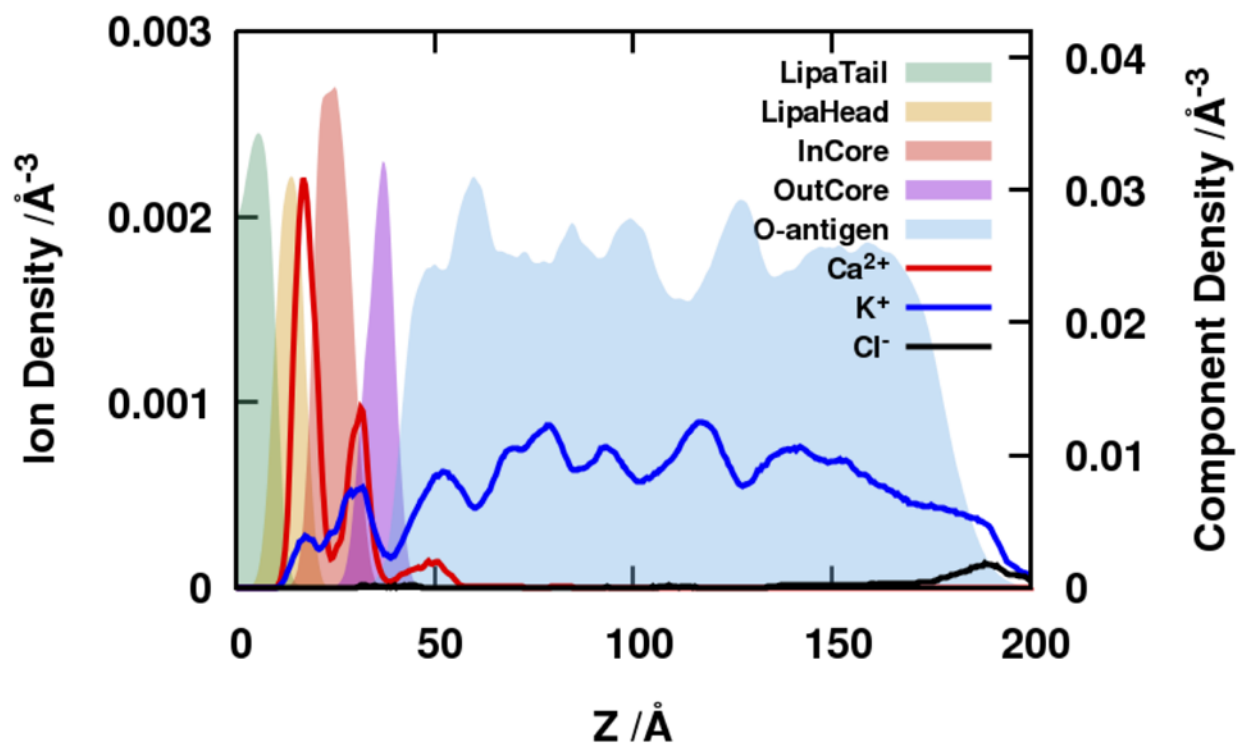
Figure 12. Distributions of ions (Ca^{2+}, K^{+}, and Cl^{-}) along the *Z*-axis, mapping onto the heavy atoms density profiles of different LPS components in the *E. coli* O91 LPS10 bilayers. Only the membrane portion of $Z > 0$ is shown after symmetrization. K^{+} and Cl^{-} ion-density were scaled by two for clarity.
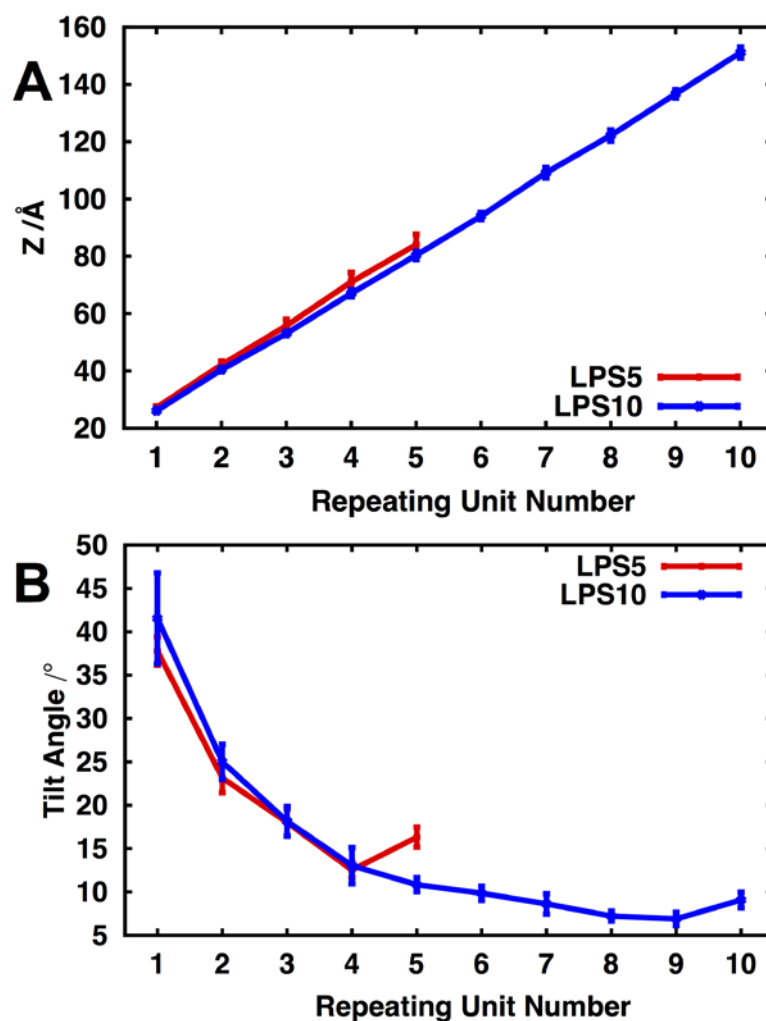
Figure 13. Conformational dynamics of *E. coli* O91 O-antigen in both LPS5 and LPS10 bilayers. (A) Average distances (with the standard errors over three independent simulations) between the lipid A phosphate groups and the first residue of each O-antigen repeating unit along the Z-axis. (B) Average tilt angles (with standard errors) of each repeating unit. The tilt angle is defined by the vector made by the first residue of RU1 and the last residue of each repeating unit with respect to the bilayer normal (Z axis).

TOC